Surface wave tomography of the western United States from ambient seismic noise: Rayleigh and Love wave phase velocity maps

Journal:	*Geophysical Journal International*
Manuscript ID:	GJI-07-0228
Manuscript Type:	Research Paper
Date Submitted by the Author:	09-May-2007
Complete List of Authors:	Lin, Fan-Chi; University of Colorado at Boulder, Physics Moschetti, Morgan; University of Colorado at Boulder, Physics Ritzwoller, Michael; University of Colorado at Boulder, Physics
Keywords:	ambient noise, Crustal structure, Surface waves, Tomography, cross-correlation, Green's function, western United States

Surface wave tomography of the western United States from ambient seismic noise: Rayleigh and Love wave phase velocity maps

Fan-Chi Lin, Morgan P. Moschetti, and Michael H. Ritzwoller

Center for Imaging the Earth's Interior
Department of Physics
University of Colorado at Boulder
Boulder, CO 80309-0390 USA
linf@colorado.edu, (303 492 0985)

Abstract

We present the results of Rayleigh wave and Love wave tomography in the western United States using ambient seismic noise observed at over 250 broadband stations from the EarthScope/USArray Transportable Array and regional networks. All available three-component time series for the 12-month span between 1 November 2005 and 31 Oct 31 2006 have been cross-correlated to yield estimated empirical Rayleigh and Love wave Green's functions. The Love wave signals were observed with higher average signal-to-noise ratio (SNR) than Rayleigh wave signals and hence can not be fully accounted by the scattering of the Rayleigh wave. Phase velocity dispersion curves for both Rayleigh and Love waves between 5 and 40 sec period were measured for each inter-station path by applying frequency-time analysis. The average uncertainty and systematic bias of the measurements are estimated using a method based on analyzing thousands of nearly linearly aligned station-triplets. We find that empirical Green's functions can be estimated accurately from the negative time derivative of the symmetric component ambient noise cross-correlation without explicit knowledge of the source distribution. The average travel time uncertainty is less than 1 sec at periods shorter than 24 sec. We invert the measurements for Rayleigh and Love wave phase speed maps at periods of 8, 12, 16, and 20 sec. The maps show clear correlations with major geological structures and qualitative agreement with previous results based on Rayleigh wave group speeds.

1. Introduction

Surface-wave tomography using ambient seismic noise, also called ambient noise tomography (ANT), is becoming an increasingly well established method to estimate short period (< 20 sec) and intermediate period (between 20 and 50 sec) surface wave speeds on both regional (Sabra et al., 2005a; Shapiro et al., 2005; Kang and Shin, 2006; Yao et al., 2006; Lin et al., 2007; Moschetti et al., 2007) and continental (Yang et al., 2007; Bensen et al., 2007b) scales. The applicability of the method at long periods (> 50 sec) is also now receiving more attention (e.g., Yang et al., 2007; Bensen et al., 2007a). In these studies, Rayleigh wave Green's functions between station-pairs are estimated by cross-correlating long time-sequences of ambient noise recorded simultaneously at both stations. These studies have established that, within reasonable tolerances, the measurements are repeatable when performed in different seasons, the Green's functions agree with earthquake records, dispersion curves agree with those measured from earthquakes, and the resulting tomography maps cohere with known geological structures such as sedimentary basins and mountain ranges. Applied to regional array data, such as the EarthScope/USArray Transportable Array (TA), PASSCAL experiments, or the Virtual European Broadband Seismic Network, the resulting dispersion maps display higher resolution and are obtained to much shorter periods than those typically derived from teleseismic earthquakes. This holds out the prospect to infer considerably higher resolution information about the crust and uppermost mantle over extended regions.

To date, these studies have concentrated exclusively on Rayleigh waves and predominantly have used the estimated empirical Green's functions to obtain only measurements of group speed. Yao et al. (2006) was the first to use the empirical Green's functions to estimate the Rayleigh wave phase speed. The first principle purpose of this paper is to investigate the extension of ambient noise tomography to Love waves and to make phase measurements in the western United States. In so doing, we use data from the EarthScope/USArray TA combined with other regional networks in the western United States. From its inception until 31 October 2006, over 250 TA stations were deployed in this region and operated for various lengths of time (Figure 1). Moschetti et al. (2007) have used these stations recently to obtain Rayleigh wave group velocity maps at periods from 8 to 40 sec using ANT. We explicitly extend this study to phase velocity measurements and also show for the first time that Love wave dispersion also can be measured from ambient noise and be used to produce tomographic maps.

Early ambient noise studies focused on Rayleigh waves at the expense of Love waves because of the higher locally generated noise on the horizontal components and general skepticism that the ambient noise source would be ineffective at directly generating Love waves. Numerous ambient noise source studies (e.g., Rhie and Romanowicz, 2004, 2006; Stehly et al., 2006) have concluded that coupling between ocean waves and the shallow seafloor produces long-range coherent noise on the vertical component. It has been believed, however, that it is more difficult to couple ocean waves with horizontal motions of the seafloor, which would make Love wave generation less efficient than that of Rayleigh waves. We show here that, in fact, Love waves appear clearly on the transverse-transverse cross-correlations between most station pairs, at least at periods shorter than 20 sec.

The ability to make both Rayleigh and Love wave dispersion measurements at periods shorter than ~20 seconds is important if radial anisotropy (the bifurcation of Vsv and Vsh) in the crust is to be observed. Shapiro et al. (2004) inferred strong radial anisotropy in the Tibetan crust, which they argued is caused by on-going crustal deformation. This inference is based on observing a discrepancy in the dispersion characteristics of Rayleigh and Love waves at periods for which the waves are sensitive to the crust. The thick crust of Tibet means that surface waves retain sensitivity to crustal structures to much longer periods than elsewhere in the world. For a crustal Rayleigh-Love discrepancy to be observed across the western US, for example, where the average crustal thickness is less than half that of Tibet, Rayleigh and Love wave dispersion should be obtained to periods down to at least 10 sec. Such periods are attenuated strongly from distant earthquakes and are largely unobservable, but are readily observed with ambient noise.

Past work also has concentrated on group rather than phase velocities for a number of reasons, perhaps most importantly because the "initial phase" of ambient noise is not well understood and has been the subject of some speculation and confusion. Theoretical work done by Lobkis & Weaver (2001), Roux et al. (2005), Sabra et al. (2005b), and Snieder (2004) suggested that phase information in the surface-wave Green's function can be recovered from the negative time derivative of the symmetric cross-correlation under the assumption of a spatially homogeneous ambient-noise source distribution. (The "symmetric component cross-correlation" or "symmetric signal" is the average of the cross-correlation at positive and negative correlation lag times.) Under this assumption, Yao et al. (2006) presented the first phase speed tomography based on ambient noise over south-east Tibet. However, how this assumption may alter, degrade or break-down given the inhomogeneous distribution of ambient noise sources on earth has been unclear. The inhomogeneous distribution of noise sources is seen clearly by comparing the positive and negative lags of the cross-correlations (e.g., Lin et al., 2007). This type of observation is the basis for recent studies aimed at characterizing ambient noise sources (e.g., Stehly et al., 2006; Yang & Ritzwoller, 2007). Yao et al. (2006) have also suggested that an inhomogeneous source distribution may account for part of the 1% – 3% inconsistency they observed between phase velocity measurements made by the ambient noise method and the traditional earthquake-based two-station method between periods of 20 - 30 sec.

Phase velocity measurements are desirable for the following reasons. First, as we show, the uncertainty of the phase velocity measurement is much smaller than that of the group velocity measurement. Second, within the same period band, phase velocity has a deeper sensitivity kernel and, therefore, constrains deeper velocity structures. Third, the dispersion relation for group velocity can be calculated from the dispersion relation of phase velocity, but the converse is not true.

The second principal purpose of this paper is to address whether robust phase velocity measurements can be obtained from ambient noise without explicit knowledge of the source distribution. We use an empirical three-station method, discussed in section 4.2, to test this hypothesis and also to identify systematic errors and the average uncertainty of real phase velocity measurements. Several previous studies have used seasonal variability to estimate the uncertainty of the measurements (e.g., Lin et al., 2007; Bensen et al., 2007a; Yang et al., 2007).

Our method, however, avoids the possibility of repeated false measurements and systematic error. Synthetic cross-correlations based on different source distributions, discussed in Section 6.2, suggest that the initial phase of the estimated Green's function would be approximately zero if the source distribution were to vary smoothly over the constructive interference region. Combined with the result of the three-station method, we show that even though ambient noise sources have an inhomogeneous azimuthal distribution, ambient noise is distributed sufficiently homogeneously so that no additional phase shift is required in the estimated Green's function to account for irregularities in the source distribution.

We describe the method to obtain the estimated Green's functions for both Rayleigh and Love waves in section 2. Evidence for the existence and retrievability of Love waves is presented in section 3. In section 4, we describe the method used to obtain the phase velocity measurements and the three-station method developed to estimate the systematic errors and the average uncertainty of the measurements. Tomography maps at periods of 8, 12, 16, and 20 sec for both Rayleigh and Love wave phase speeds are presented in section 5. Throughout the paper, we focus on phase velocity measurements between periods of 8 and 24 sec, where the highest signal-to-noise ratios are observed, on average.

2. Data Processing to Produce the Estimated Green's Functions

We analyzed continuous data from over 250 broadband stations in the western US recorded between 1 November 2005 and 31 October 2006. Data from all three components (East, North, Vertical) were used, and cross-correlations between all possible pairs of components from the two-stations were computed. The method to obtain the estimated Green's function is similar to that described for Rayleigh waves by Bensen et al. (2007a). We summarize it briefly here with a concentration on the Love wave data processing.

All data are processed on a daily basis and then are stacked (superposed and added together) later. The mean, trend, and instrument response of the daily component (E, N, Z) seismograms are first removed and band-pass filtered between periods of 5 sec and 100 sec. To speed up the process, we do not rotate the components into the radial (R) and transverse (T) directions for each station-pair until the component cross-correlations (E-E, E-N, N-N, N-E) are performed. Earthquake signals and instrumental irregularities are then removed by temporal normalization. In order to postpone the component rotation until after cross-correlation, the East and North components are temporally normalized together. To achieve this, both components are first band-pass filtered between 15 sec and 50 sec, a band that contains the most energetic surface wave signals from earthquakes. For each time point, the mean of the absolute value of each seismogram is computed in the 128 second window centered on that point. The values of the East and North components are compared, and the larger is used to define the inverse weight for that time point. That weight is then applied to both the North and East component time-series band-passed between 5 sec to 100 sec. This process effectively suppresses earthquake signals and maintains the linearity of the rotation operator.

After temporal normalization, the signals are whitened in frequency. Before whitening, ambient noise is most energetic in the microseismic band below 20 sec period. Frequency whitening is carried out to broaden the period band of the dispersion measurement. Again, to maintain the linearity of the rotation operator, the East and North signals are whitened together. Because the spectra of both components are similar, on average, we do this by simply weighting the East and North signals in the frequency domain by the inverse of the smoothed East spectrum. Other methods, such as weighting by the mean of the two spectra or their product produce similar results. This concludes the data preparation prior to cross-correlation.

North-North, North-East, East-East and East-North cross-correlations are calculated between every station-pair for each day-length record. We stack all available daily cross-correlations for each station-pair into one time-series to enhance the signal-to-noise ratio (SNR). Because all processes are linear in the rotation operator, the transverse-transverse, transverse-radial, radial-radial, and radial-transverse cross-correlations between each station-pair can be calculated by a linear combination of those four components with coefficients related to the inter-station azimuth θ and back-azimuth ψ angles. These angles are defined by setting the first station as the "event" location and the second station as the receiver location so that the rotation is:

$$\begin{pmatrix} TT \\ RR \\ TR \\ RT \end{pmatrix} = \begin{pmatrix} -\cos\theta\cos\psi & \cos\theta\sin\psi & -\sin\theta\sin\psi & \sin\theta\cos\psi \\ -\sin\theta\sin\psi & -\sin\theta\cos\psi & -\cos\theta\cos\psi & -\cos\theta\sin\psi \\ -\cos\theta\sin\psi & -\cos\theta\cos\psi & \sin\theta\cos\psi & \sin\theta\sin\psi \\ -\sin\theta\cos\psi & \sin\theta\sin\psi & \cos\theta\sin\psi & -\cos\theta\cos\psi \end{pmatrix} \begin{pmatrix} EE \\ EN \\ NN \\ NE \end{pmatrix} \qquad (1)$$

Note that both the radial components and the transverse components at both stations point to the same direction respectively under our notation as shown in Figure 2.

An example of the resulting cross-correlation between stations 116A and R06C is shown in Figure 3. Both causal and acausal signals at positive and negative correlation lag times, respectively, are observed, corresponding to waves propagating in opposite directions between the stations. A clear difference in arrival time is observed between the waveforms on the transverse-transverse (T-T) and radial-radial (R-R) cross-correlations. Signal arrival times on the vertical-vertical (Z-Z) cross-correlation and the R-R cross-correlation are similar, and result from the Rayleigh wave. The T-T cross-correlation exhibits the faster Love wave arrival. Although both the Z-Z and R-R cross-correlations contain the same Rayleigh wave signal, the Z-Z cross-correlation generally has a higher SNR. Hence, like others before us, we focus on using Z-Z cross-correlations for the Rayleigh wave analysis.

Using the spatial reciprocity of the Green's functions, we average the positive and negative lag signals to obtain the "symmetric-signal" of the cross-correlation. In most cases, this enhances the SNR and also effectively mixes the signals coming from opposite directions, which helps to homogenize the source distribution. The estimated Green's function between stations A and B, $G_{AB}(t)$, is then obtained by taking the negative of the time-derivative of the symmetric signal cross-correlation, $C_{AB}(t)$:

$$G_{AB}(t) = -\frac{d}{dt}\left[\frac{C_{AB}(t)+C_{AB}(-t)}{2}\right] \qquad 0 \le t < \infty . \tag{2}$$

This time-derivative and the sign-flip do not affect the group speed but do alter the signal phase and, hence, the measured phase speed. Without this operation, the symmetric cross-correlation can be thought of as the response due to an impulsive displacement. The traditional definition of the Green's function, however, is the system response to an impulsive force, which is out of phase with displacement by $\pi/2$. In the following, it will be important to remember this phase difference between the cross-correlation and the empirical Green's function. In Bensen et al. (2007a), the cross-correlation was mistakenly identified with the estimated Green's function. Although both the phase and group velocity analyses based on the Green's function remain correct in the paper, to get unbiased measurements, the cross correlation must first be transformed to the empirical Green's function by using equation (2) above.

The choice to rotate the North and East components into the transverse and radial components after cross-correlation makes the computation considerably more efficient and space saving. We compared the result of both cases and no difference was observed.

3. Existence and Strength of Love waves in Ambient Noise

Figures 4a and 4b show record sections centered at the station MOD (Modoc Plateau, CA) for the Rayleigh wave (Z-Z) and the Love wave (T-T), respectively. Signals emerged at both positive and negative correlation lags for Rayleigh and Love waves and Rayleigh waves clearly travel slower than Love waves, as expected. Love waves, in fact, are commonly observed on cross-correlations across the western US.

In order to quantify the strength of the signals, for each station-pair we calculate the spectral signal-to-noise ratio (SNR) by computing the ratio of the signal peak in the predicted arrival window to the root mean square (rms) of the noise trailing the arrival window in each period band for the symmetric component cross-correlation. The prediction window is defined by assuming that the waves travel between 2 to 5 km/s (Figure 3), and the noise window starts 500 seconds after the prediction window and ends at 2700 seconds lag time. The resulting average SNR for all the station pairs with inter-station distance larger than three wavelengths is shown in Figure 5, where a phase speed of 4 km/s is used to compute the wavelength here and elsewhere.

The most surprising feature observed in Figure 5 is that Love waves exhibit higher average SNR than Rayleigh waves, especially between about 10 to 20 sec period. This suggests that Love waves cannot be generated exclusively by the scattering of Rayleigh waves. Moreover, the SNR of the Rayleigh wave for both the Z-Z and R-R cross-correlations exhibits two peaks that correspond to the 8 sec (secondary) and 16 sec (primary) microseisms, respectively. On the other hand, the Love wave only shows a single peak around a period of 14 sec which suggests that the origin of Rayleigh and Love waves may differ in some way.

The SNR drops rapidly for the Love waves above 20 sec period, in contrast with the slow drop-off in SNR for the Rayleigh wave on the Z-Z component. However, on the R-R component, the Rayleigh wave SNR remains lower than that of the Love wave up to 40 sec period where little signal is detected. This indicates that the horizontal components of the seismograms are heavy contaminated by non-coherent local noise. The drop-off of SNR of Love waves above 20 sec period may, therefore, arise from the growth of incoherent local noise rather than the decay of the signal with increasing period. Further investigation of the physical mechanisms as well as the locations of the source of Love wave ambient noise is important to address, but is beyond the scope of this paper.

4. Phase Velocity Measurement

All data processing described hereafter begins with the estimated Green's functions obtained from the symmetric component of the cross-correlations by applying a negative time-derivative. We used the Z-Z and T-T cross-correlations to obtain the estimated Rayleigh and Love wave Green's functions for each station pair. With the choice of the direction we made on the transverse component (Figure 2), the Rayleigh and Love wave Green's functions have the same form and the same phase velocity analysis can be applied to both Rayleigh and Love waves.

4.1 Frequency-Time Analysis

We obtained the Rayleigh wave and Love wave phase velocity dispersion curves by automated frequency-time analysis (FTAN) (Bensen et al., 2007a). First, FTAN applies a series of Gaussian band-pass filters to the estimated Green's function. The resulting waveform $f(t)$ at each period can be combined with $+iF_H(t)$ to form a complex function $A(t)\exp[i\varphi(t)]$, where $F_H(t)$ is the Hilbert transform of $f(t)$, $A(t)$ is the envelope function, and $\varphi(t)$ is the phase function. We note that the choice of the positive sign of $+iF_H(t)$ results in a decrease of phase with an increase in time. This choice is somewhat arbitrary; but must be consistent with the theoretical phase as shown in the equation (3) below. After obtaining the envelope and phase functions, the group travel time, t_{max}, is measured directly as the peak of the envelope function, and the group velocity is simply r/t_{max}, where r is the distance between the two stations. The corresponding instantaneous frequency at t_{max} is determined by taking $\omega = \left[\frac{\partial \varphi(t)}{\partial t}\right]_{t=t_{\max}}$, which deviates from the center frequency of the Gaussian band-pass filter slightly. Theoretically, for an instantaneous frequency ω the phase of the estimated Green's function observed at time t can be expressed as:

$$\varphi(t) = kr - \omega t + \frac{\pi}{2} - \frac{\pi}{4} + N \cdot 2\pi + \lambda \qquad N \in Integer, \lambda \in \mathrm{Re} \qquad (3)$$

where k is the wave number, $\pi/2$ is the phase shift from the negative time-derivative, $-\pi/4$ is the phase shift due to the interference of a homogeneous source distribution (discussed further in section 6.2 below), $N \cdot 2\pi$ is the intrinsic phase ambiguity of phase measurement, and λ is the source phase ambiguity term or "initial phase" that arises from the uncertainty of the source distribution in addition to other factors.

Note that under the theoretical expectation of the Green's function which is the displacement response due to a point force impulse, the $\pi/2$ phase shift accounts for the phase shift between the displacement and the force and the $-\pi/4$ phase shift is the asymptotic remnant of the Bessel function under the far-field approximation. Further discussion on how the -π/4 phase term arises and how λ may depend on the source distribution appears in section 6.2.

From equation (3), the phase velocity *c* when measured on the empirical Green's function is given by

$$c = \frac{\omega}{k} = \frac{r\omega}{\left[\varphi(t_{\max}) + \omega t_{\max} - \frac{\pi}{4} - N \cdot 2\pi - \lambda\right]} \quad . \qquad (4)$$

In equation (4), *N* and λ are still unknowns, however. In order to obtain a reliable, unambiguous phase velocity measurement both, *N* and λ are needed. As we will discuss, *N* is an integer that can be determined unambiguously in the vast majority of cases. The source phase ambiguity factor λ, however, can be any real number and also can be frequency dependent. It is, therefore, more difficult to constrain, and its determination is the subject of section 4.2.

At long periods (> 20 s), *N* can be resolved easily by comparing the resulting measurement with previous phase velocity studies based on earthquake data. Figure 6 shows an example of dispersion curves obtained from cross-correlation of data from stations CVS and VES in

California with various different N value and with λ=0. Here, we used the average phase velocity curve determined by Yang & Forsyth (2006) in Southern California as the reference curve for the Rayleigh waves. No suitable Love wave reference curve exists, so we increased the Rayleigh wave curve by 9% to give the Love wave reference. By applying a smoothness constraint to the dispersion curves, N at shorter periods (< 20 s) can also be resolved. The same method does not work for λ however.

4.2 Three-Station Method: Determination of λ

Theoretical studies have predicted that the initial phase, λ, should equal zero under the assumption of a homogeneous source distribution (e.g., Sneider 2004; Roux et al. 2005). There is, however, strong observational evidence that the strength of ambient noise is azimuthally heterogeneous (e.g., Shapiro et al., 2006; Stehly et al., 2006). It is, therefore, necessary to determine the value of λ empirically. To do this, we compare the phase travel time (or delay) between station-triples that are nearly aligned along the same great-circle. In general, such station-triples are hard to find, but the TA component of EarthScope/USArray has been laid out approximately on a square grid and many such near station-triples exist. It is the ideal network configuration to resolve this problem.

The idea is as follows. Consider a station-triple that is composed of three nearly co-linear stations A, B, and C, as shown in Figure 7a, where station B lies between stations A and C. Stations A and B are separated by a distance d2, B and C are separated by a distance d3, and A and C are separated by a distance d1. The distance d1 is nearly but not identically equal to the sum of the distances d2 and d3. If there is no initial phase term for all cases (i.e., if $\lambda = 0$), then the sum of the observed phase times taken on the short-legs, stations A-B and B-C, will approximately equal the phase time observed on the long-leg; i.e., between the outside stations, A-C. Thus, $t1 \approx t2 + t3$. If, however, there is a non-zero initial phase ($\lambda \neq 0$), there will be a difference between the sum of the phase times on the short-legs and that on the long-leg: $t1 \neq t2 + t3$. To interpret each individual deviation is not practical. However, the bulk statistics can be interpreted to produce an estimate of λ. In addition, this three-station method provides information about measurement uncertainties and possible systematic bias.

In performing this analysis, the difference in distance between the sum of the two shorter legs (*d2+d3* in Figure 7a) and the longest leg (*d1* in Figure 7a) is limited to less than 50 km. Also, to limit ourselves to reliable velocity measurements but retain a sufficient number of measurements for statistical analysis, two selection criteria are used. First, the distance between each station-pair in a triple must exceed 2 wavelengths to satisfy the far-field approximation. Again, a phase velocity of 4 km/s is used to estimate the wavelength. Second, the SNR at the period of interest must be greater than 15 for all three pairs of stations for the triple to be included in the analysis.

The relationship between *(d2+d3)-d1*, or Δd, and *(t2+t3)-t1*, or Δt, at a period of 18 sec for all the station-triples that satisfy the above conditions, 2124 in total, is plotted as an example in Figure 7b. A clear trend is seen, with Δt increasing as Δd increases. To account for this slope, a corrected travel time difference $\Delta t'$ is computed as follows

$$\Delta t' = \frac{d1 \cdot (t2 + t3)}{d2 + d3} - t1 \tag{5}$$

Here, $\frac{t2 + t3}{d2 + d3}$ can be considered as the average slowness for the wave traveling through *d2* and *d3*. The relationship between Δd and $\Delta t'$ is plotted in Figure 7c, where we have set $\lambda = 0$. The majority of the measurements aggregate near $\Delta t'$ =0, although there is substantial scatter, particularly as Δd grows. When the initial phase $\lambda = -\pi/4$, the result is presented in Figure 7d for comparison. In this case, most of the $\Delta t'$ shift by 2.25 sec to the right and the majority of the $\Delta t'$ clearly deviate from zero. This deviation indicates a systematic bias in the measurement, in this case caused by the wrong value of λ. The most egregiously scattered points, around 2% of the total points if defined by $\left|\Delta t' - \overline{\Delta t'}\right| > 10$ sec, in Figure 7c and 7d result from the wrong choice of the value of N in equation (3). This set of points actually changes when different values of the initial phase λ are used. For example, when λ = -π/4, a set of measurements with $\Delta t'$ ~20 sec are introduced. In these cases, the $\Delta t'$ do not simply shift by 2.25 sec, but the statistics of the distribution are changed very little.

Results for the corrected travel-time difference between the long-leg and the sum of the two shorter legs, $\Delta t'$, for the 12, 18, and 24 sec period Rayleigh waves and the 12 and 18 sec Love waves are summarized with histograms in Figure 8a-d. The number of station-triples that pass the selection criteria is too small to be considered statistically significant for the 24 sec Love wave. The standard deviation (STDV) and the mean value of the Gaussian fit to these histograms are summarized in Table 1. Results for initial phase λ = 0 and -π/4 are used again for comparison. For both Rayleigh and Love waves, with λ = -π/4, the mean of the Gaussian fit clearly deviates from zero and the deviation increases with period. On the other hand, the deviation from zero is small with $\lambda = 0$ for all cases and no trend with period is observed. From Table 1, we conclude that if $\lambda = 0$ is applied, the systematic bias in the phase measurements is negligible.

We can also estimate the average uncertainty of the measurements from Table 1. If we assume that the three phase travel times t1, t2, and t3 are independent measurements, the average uncertainty of each individual travel time measurement can then be estimated with $\frac{1}{\sqrt{3}}\sigma$, where σ is the STDV in the Gaussian fit. The average phase time uncertainty increases with increasing period as expected, but is less than 1 second for most cases. An uncertainty of less than half a second would be impossible to attain because 1 sample per second time series are used in this study. This estimation of the uncertainty is independent of the repeatability of the measurements at different times, which has been performed in other studies (e.g., Yang et al., 2007; Bensen et al., 2007a), and provides a new way to estimate the average travel time uncertainty. This uncertainty, however, is characteristic of the inter-station spacings used in this study, and would be expected to grow with increasing inter-station distance.

The three-station method developed here confirms that $\lambda = 0$ is a good approximation for the majority of the measurements. The results also provide insight into the quality of the phase velocity measurements. Overall, the phase travel time measurements in this study display a negligible systematic error and an average uncertainty of less than 1 second for periods shorter than 24 sec. The implication of these results for the distribution of ambient noise sources is discussed in section 6.2.

As an example of the result Rayleigh and Love wave phase velocity measurements, Figure 9 shows two sets of symmetric component cross correlations and the resulting phase velocity dispersion curves. The path between O01C (Eel River Conservation Camp, CA) and R04C (Big Horse Ranch, CA) goes through the Sacramento Basin and the path between ORV (Oroville Dam, CA) and TIN (Tinemaha, CA) goes through the Sierra Nevada. A clear velocity contrast at short periods (<15 sec) due to the variation of sediment thickness is observed between O01C–R04C and ORV–TIN. The rapid increase of the phase velocity with the period for O01C–RO4C between 10–20 sec is a characteristic feature of thin crust. On the other hand, an almost flat dispersion curve, such as that for ORV–TIN shown here, usually represents a thicker crust. In both cases, the Love wave measurements consistently exhibit higher phase velocities than the Rayleigh wave measurements and approach to our reference models at long periods.

5. Phase Velocity Tomography for Rayleigh and Love Waves

The selection of the most reliable measurements for tomography is based on three criteria. First, the distance between two stations must be longer than 3 wavelengths to satisfy the far-field approximation. Again, 4 km/s is used as a rule-of-thumb to estimate the wavelength. This introduces an effective long-period cut-off of r/12 (in seconds) between stations separated by distance r in km. For example, stations separated by 120 km will not return measurements at periods greater than 10 sec. Second, the SNR must be higher than 17 at the period of interest. Third, each measurement must be coherent with other measurements as measured by its ability to be fit by a tomographic map.

Figure 10 shows the number of measurements satisfying the first two selection criteria out of the 32,131 station-pairs for both Rayleigh and Love waves at different periods. The shapes of the curves are very similar to the average SNR curves shown in Figure 5. At periods above 20 sec, both the R-R Rayleigh and T-T Love wave signals presumably have been obscured by high local noise levels on the horizontal component of the seismogram. This limits the longest period of Love wave tomography in this study to about 20 sec. The lower local noise on the vertical component allows us to extend the tomography for Rayleigh waves to significantly longer periods.

We inverted the phase velocity measurements for both Rayleigh and Love waves at 8, 12, 16, and 20 sec period for phase speed maps using the tomographic method described by Barmin et al. (2001). The method estimates isotropic wave speed by minimizing a penalty functional composed of data misfit, model smoothness, and the perturbation $\mathbf{m}$ to an input reference model, $\mathbf{m}_o$,weighted by local path density. Here, we used the average of all selected velocity measurements at each period as our reference model $\mathbf{m}_{o.}$ The method effectively employs "fat rays", similar to the use of Gaussian beams. Ritzwoller et al. (2002) showed that diffraction tomography with finite frequency sensitivity kernels recovers similar structure to this version of ray theory at periods shorter than 50 sec in most continental regions with dense path coverage. We have no reason to believe that more sophisticated finite-frequency kernels would change the results presented here appreciably, particularly in light of uncertainties in the shape of such kernels, the short periods considered here, and the short inter-station paths compared to teleseismic path lengths.

Figures 11a and 11c show the typical path coverage for Rayleigh and Love waves, respectively, in the inversion. Figures 11b and 11d show the resulting resolution maps estimated with the method described by Barmin et al. (2001) with modifications presented by Levshin et al. (2005). For each point on the map, the resolution surface resulting from the resolution matrix is fit locally by a 2-D Gaussian function and twice the estimated standard-deviation is identified with the estimated resolution. The resolution across most of the western US is smaller than 70 km, approximately equal to the average inter-station spacing, as expected for good data coverage.

A third data selection criterion must be satisfied by the data. Using data satisfying the first two criteria, we invert for a preliminary over-smoothed map at each period. All the measurements with travel time residuals larger than 6 seconds were removed from the data set. This process removed around 4%, 3%, 1%, and 1% of the data for the Rayeigh waves at 8, 12, 16 and 20 sec and 7%, 6%, 4% and 2% for the Love waves, respectively. More measurements were removed at shorter periods mainly due to the lack of a reliable reference model to solve the 2π phase ambiguity and the larger velocity variations that result from structural variations at short periods. Without a good reference model at short periods, it is easier to select the wrong branch (*N* value) than long periods in the phase velocity measurement.

Examples of the resulting tomography maps are shown in Figures 12 and 13. The tomography maps at 8, 12, 16, and 20 sec for both Rayleigh waves and Love waves are shown. The black contour plotted on each map encloses the region with an estimated resolution less than 100 km. Any features outside this contour should be interpreted with caution. The misfit of the tomography maps to the data is summarized in Figure 14. The small standard deviations (STDV) of the misfits indicate good coherence between the measurements, on average. The gradual increase in STDV with decreasing period reflects stronger heterogeneity in the shallower crust.

6. Discussion

6.1 Phase velocity maps for Rayleigh and Love waves

As an aid to guide the qualitative interpretation of the phase velocity maps, Figure 15 displays the radial sensitivity kernels for Rayleigh and Love waves based on PREM in which the ocean is replaced by a sedimentary layer.

The 8 sec Love wave map is most sensitive to the upper 10 km of the crust and represents the shallowest structure in all cases. The fast anomaly of the Sierra Nevada and the slow anomaly of the Central Valley are the most profound features in the 8 sec Love wave map.

The 12 sec Love wave and 8 sec Rayleigh wave maps are both sensitive to slightly deeper structures and image very similar features, as expected. Again, the fast anomaly of the Sierra Nevada is seen, but the Central Valley anomaly starts to separate into the Sacramento Basin in the north and the San Joaquin Basin in the south. The fast anomaly of the Cascade Range begins to appear from northern California through Washington.

The 12 sec and 16 sec Rayleigh wave and 16 sec and 20 sec Love wave maps consistently exhibit similar features. The major slow anomaly of the Central Valley region gradually disappears with increasing period because the surface waves begin to sense the faster shear wave speeds in the crystalline rocks in the underlying basement, and the slow shear wave speeds of the sediment layer are compensated by higher velocities below. In the 20 sec Rayleigh wave map, the opposite effect can be seen in the Sierra Nevada region. Due to relatively thick crust, the fast anomaly at shorter periods turns to a slower anomaly at longer periods.

These results are in general agreement with previous studies. Moschetti et al. (2007) observed the Rayleigh wave group velocity dispersion in the same region with ambient noise tomography. In general, the phase velocity measurements are sensitive to slightly deeper structures compared to group velocities at the same period. Comparing the 8 sec, 16 sec, and 24 sec Rayleigh wave group velocity maps of Moschetti et al. with our 8 sec, 12 sec, and 20 sec Rayleigh wave phase velocity maps, respectively, a striking similarity is observed. Also, there are very similar features on our 25 sec Rayleigh wave map (not shown here) with the one reported by Yang and Forsyth (2006) in Southern California, which was constructed using the two plane wave method with teleseismic earthquakes. In Yao et al. (2006), a 1.5%–3% systematic bias between Rayleigh wave phase velocities between 20–30 sec period measured by the ambient noise method and the earthquake-based two station method was reported. We compare our mean speed in the Southern California with that obtained by Yang and Forsyth (2006), the difference is less than 0.5%.

6.2 Implications for the Distribution of Ambient Noise Sources

The source phase ambiguity term or "initial phase" λ in the equation (3) was introduced to account for the phase shift due to a possibly azimuthally inhomogeneous distribution of ambient noise sources. We discuss here how source distribution is expected to affect the phase of the cross-correlation and then draw conclusions about ambient noise source distribution from the three-station method discussed in section 4.2.

For a single source cross-correlation, when a homogeneous medium is considered, the initial phase of this cross-correlation at a particular instantaneous frequency is purely determined by the distance difference between the source and the two stations. In consequence, source locations with the same initial phase will lie along hyperbolas with foci at the two stations. Figure 16 shows an example of the iso-phase hyperbolas at 50 sec period with stations separated by 1000 km where the initial phase of each neighboring hyperbola differs by π. Over most of the region, the initial phase is sensitive to even slight changes in the azimuth angle so that when multiple sources are present, destructive interference occurs. The areas with highly stable initial phase occur where the distance between the hyperbola are large. These regions, where sources will interefere constructively, are located on the outward sides of the two stations near the line connecting them. If sources were located exclusively along the outward lines linking the two stations, then the uniform constructive interference between these sources would be completely in phase and the $-\pi/4$ that appears in equation (3) would need to be removed. In this case, the initial phase $\lambda = \pi/4$. In contrast, for an azimuthally homogeneous source distribution, the resulting constructive interference in the two outward areas together with the destructive interference for sources elsewhere result in a $-\pi/4$ phase shift in the cross-correlation relative to if the sources are only located on the outgoing parts of the line connecting the two stations. This phase shift corresponds to the $-\pi/4$ in the equation (3) and $\lambda = 0$ in this case. Analytical proof of this phase shift by using the stationary phase approximation can be found in Sneider (2004).

Through our three station analysis, described in section 4.2 above, we concluded that with λ=0 systematic measurement bias is negligible, with an average travel time uncertainty of about 1 second. This sets an upper bound for the uncertainty of the phase ambiguity λ near $\pi/10$ or one-twentieth of a cycle, since measurement error also contributes to the uncertainty of the measurement. How this small uncertainty of λ fits into the apparently inhomogeneous source distribution around the global is a nontrivial question. We present here three synthetic experiments based on different source distributions to provide some insight.

In Case 1, synthetic sources are distributed randomly in a 5000 km $\times$ 5000 km square area and the receivers are placed 1000 km apart, as shown in Figure 16. In this case, with λ =0, our measurement procedure is expected to return the input phase velocity. In Case 2, the sources are randomly distributed, but are confined to the line connecting the stations. Instead of λ =0, we expect to measure phase with $\lambda = +\pi/4$. In Case 3, the synthetic sources are randomly distributed in the grey area showed in Figure 16. We choose 3 km/s as an input phase velocity for a non-dispersive, non-attenuative homogeneous medium. Each synthetic source emits a Gaussian like wavefront with a 3 second width propagating outward with a random initial time and random polarity. Here, the first two cases are focused on confirming the method and the idea of initial phase and the third case is our preferred model of ambient noise source distribution.

The resulting 5-100 sec band-pass cross-correlation functions for all cases are shown in Figure 17a. Clear signals are observed on all three cross-correlations. In Case 3, the signals are only observed at positive lag time due to the asymmetry of the source distribution; all sources are to the left of both stations. Note that even without any sources on the right, the cross-correlations between different sources destructively interfere and appear as a background noise at negative lag time. The signals for all three cases peak at exactly the same lag times due to the constancy of group velocity, but the shape of the signal in Case 2 differs from that in Cases 1 and 3. This is due to the initial phase shift in at all frequencies. On the other hand, no clear difference in phase between Case 1 and Case 3 is observed.

The phase velocity dispersion curves measured by FTAN are shown in Figure 17b for all three cases. The medium is non-dispersive, so the group and phase speeds are the same. The velocity dispersion curves for Case 1 and Case 2 confirm our method and the idea of how initial phase depends on the source distribution. When $\lambda = 0$ and $\lambda = +\pi/4$ is applied on Case 1 and Case 2, respectively, the measured phase velocities match the input phase velocity (3 km/s) at all periods with errors less than 1%. At the same time, similar results are obtained when $\lambda = 0$ is used in the Case 3, although the source distribution is highly inhomogeneous. An example of the effect of using the incorrect initial phase is also shown by using $\lambda = 0$ in Case 2. The measured phase velocity dispersion curve clearly deviates from the input value and the error increases with period.

For comparison, the group velocity dispersion curves are also shown here in Figure 17c and exhibit the intrinsic uncertainty difference between these two kinds of measurement. Group velocity clearly exhibits higher uncertainty and the uncertainty tends to increase with the period, although non-dispersive signals are particularly hard targets for group velocity. Note that the group velocity measurement is not λ dependent; hence even with incorrect initial phase $\lambda = 0$ for case 2, the same result is returned.

Ambient noise source studies have concluded that the interaction between ocean waves and the shallow sea floor is a major mechanism to create ambient noise. Other than a few special cases, such as the 26 sec microseism in the Gulf of Guinea documented by Shapiro et al. (2006), there is no evidence that ambient noise is generated exclusively in highly localized area. Several theoretical studies (e.g., Webb 2007) suggest that ocean depth is a major factor in the strength of coupling between oceanic waves and the sea floor. This results in a source distribution region distributed broadly in shallow off-shore regions of the world's oceans, abstractly similar to what we suggest in Figure 16. In this case, the strength of the source varies rather smoothly across the constructive interference region on both sides of the station pair and the interference effect is effectively the same as if sources were homogeneously distributed at all azimuths. We believe that this is the setting for most of our measurements, and by setting $\lambda = 0$, the phase velocity can be measured with considerable accuracy.

6. Conclusion

Continuous three-component ambient noise data obtained between Nov 1st 2005 and Oct 31st 2006 recorded by over 250 stations in the Western United States were used to estimate both Rayleigh and Love wave empirical Green's functions between every station-pair. On the transverse-transverse cross-correlation function, the Love wave signal clearly emerges with an average SNR higher than the vertical-vertical Rayleigh wave between 10 to 20 sec period. This suggests that Love waves cannot be generated exclusively by the scattering of Rayleigh waves. Above 20 sec period, the Love wave SNR drops off quickly, likely due to the increase in incoherent local noise levels on the horizontal components. Further research is needed to determine whether by combining with barometric data, the local noise level can be ameliorated and longer period Love wave empirical Green's functions can be obtained from ambient noise.

The phase velocity dispersion relation between each station-pair was measured by frequency-time analysis with the initial phase, λ, in equation (3) set to 0. The consistency and average uncertainty of the measurements were determined by a novel three-station method. The results shows that the empirical Green's functions can be estimated from the negative time derivative of the symmetric component cross-correlation function without major bias and the average uncertainty of the travel time is around 1 second for periods shorter than 24 sec. The Rayleigh and Love wave phase velocity maps at four periods, 8, 12, 16 and 24 sec, were constructed and show reasonable qualitative agreement with known geological features and with previous studies. Future inversion of these data to produce a 3-D crustal model of the western United States with radial anisotropy is a natural extension of this study.

Acknowledgements

The data used in this research were obtained from the IRIS Data Management Center and originate predominantly from the Transportable Array component of USArray. This research was supported by a grant from the US National Science Foundation, grant EAR-0450082, and a contract from the US Department of Energy, contract DE-FC52-2005NA2607. MPM acknowledges a National Defense Science and Engineering Graduate Fellowship from the American Society for Engineering Education.

Reference List

Barmin, M.P., Ritzwoller, M.H. & Levshin, A.L., 2001. A fast and reliable method for surface wave tomography, *Pure Appl.Geophys.,* 158, 1351-1375.

Bensen, G.D., Ritzwoller, M.H., Barmin, M.P., Levshin, A.L., Lin, F., Moschetti, M.P., Shapiro, N.M., & Yang, Y., 2007a. Processing seismic ambient noise data to obtain reliable broad-band surface wave dispersion measurements, *Geophys. J. Int.*, 10.1111/j.1365-246X.2007.03374.x.

Bensen, G.D., Ritzwoller, M.H., & Shapiro, N.M., 2007b. Broad-band ambient noise surface wave tomography across the United States, In preparation for submission to JGR.

Kang, T.S. & Shin, J.S., 2006. Surface-wave tomography from ambient seismic noise of accelerograph networks in southern Korea, *Geophys.Res.Lett.,* 33, L17303.

Lin, F.C, Ritzwoller, M.H., Townend, J., Savage, M., & Bannister, S., 2007, Ambient noise Rayleigh wave tomography of New Zealand, *Geophys. J. Int.*, in press.

Levshin, A.L., Barmin, M.P., Ritzwoller, M.H. & Trampert, J. 2005. Minor-arc and major-arc global surface wave diffraction tomography, *Phys. Earth Planet. Int.*, **149**, 205–223.

Lobkis, O.I. & Weaver, R.L., 2001. On the emergence of the Green's function in the correlations of a diffuse field, *J.Acoust.Soc.Am.,* 110, 3011-3017.

Moschetti, M.P., Ritzwoller, M.H., & Shapiro, N.M., Surface wave tomography of the western United States from ambient seismic noise: Rayleigh wave group velocity maps, submitted to *Geochem., Geophys., Geosys.*

Rhie, J. & Romanowicz, B., 2006. A study of the relation between ocean storms and the Earth's hum, *Geochemistry Geophysics Geosystems,* 7, Q10004.

Rhie, J. & Romanowicz, B., 2004. Excitation of Earth's continuous free oscillations by atmosphere-ocean-seafloor coupling, *Nature,* 431, 552-556.

Ritzwoller, M.H., Shapiro, N.M., Barmin, M.P., & Levshin, A.L., 2002. Global surface wave diffraction tomography, *Journal of Geophysical Research-Solid Earth,* 107, 2335.

Roux, P., Sabra, K.G., Kuperman,W.A., & Roux,A., 2005. Ambient noise cross correlation in free space: Theoretical approach, *J.Acoust.Soc.Am.,* 117, 79-84.

Sabra, K.G., Gerstoft, P., Roux, P., Kuperman,W.A., & Fehler,M.C., 2005a. Surface wave tomography from microseisms in Southern California, *Geophys.Res.Lett.,* 32, L14311.

Sabra, K.G., Roux, P. & Kuperman, W.A., 2005b. Emergence rate of the time-domain Green's function from the ambient noise cross-correlation function, *J.Acoust.Soc.Am.,* 118, 3524-3531.

Shapiro, N.M., Campillo, M., Stehly, L., & Ritzwoller, M.H., 2005. High-resolution surface-wave tomography from ambient seismic noise, *Science,* 307, 1615-1618.

Shapiro, N.M., Ritzwoller, M.H. & Bensen, G.D., 2006. Source location of the 26 sec microseism from cross-correlations of ambient seismic noise, *Geophys.Res.Lett.,* 33, L18310.

Shapiro, N.M., Ritzwoller, M.H., Molnar, P., & Levin,V., 2004. Thinning and flow of Tibetan crust constrained by seismic anisotropy, *Science,* 305, 233-236.

Snieder, R., 2004. Extracting the Green's function from the correlation of coda waves: A derivation based on stationary phase, *Physical Review E,* 69, 046610.

Stehly, L., Campillo, M. & Shapiro, N.M., 2006. A study of the seismic noise from its long-range correlation properties, *Journal of Geophysical Research-Solid Earth,* 111, B10306.

Webb, S.C., 2007. The Earth's 'hum' is driven by ocean waves over the continental shelves, *Nature,* 445, 754-756.

Yang, Y. & Forsyth, D.W., 2006. Rayleigh wave phase velocities, small-scale convection, and azimuthal anisotropy beneath southern California, *Journal of Geophysical Research-Solid Earth,* 111, B07306.

Yang, Y. & Ritzwoller, M.H., 2007. The characteristics of seismic noise as a source for ambient noise tomography, in preparation.

Yang, Y., Ritzwoller, M.H.,Levshin, A.L. & Shapiro, N.M., 2007. Ambient noise Rayleigh wave tomography across Europe, *Geophysical Journal International,* 168, 259-274.

Yao, H.J., van der Hilst, R.D. & de Hoop, M.V., 2006. Surface-wave array tomography in SE Tibet from ambient seismic noise and two-station analysis - I. Phase velocity maps, *Geophysical Journal International,* 166, 732-744.

Figure Captions

Figure 1. Location of the 254 broadband stations used in this study. The color code indicates the duration of the deployment during this study.

Figure 2. The diagram on how transverse and radial components are defined.

Figure 3. The 10-25 sec band-pass filtered cross-correlation observed between two EarthScope/USArray TA stations, 116A (Eloy, Arizona) and R06C (Coleville, California). The prediction windows used for SNR analysis, defined for arrivals with velocities between 2 and 5

km/s, are marked in gray.

Figure 4. The 10-50 sec band-pass filtered record section centered at station MOD (Modoc Plateau, California) with (a) vertical-vertical cross-correlations and (b) transverse-transverse cross-correlations. The dashed lines in (a) and (b) indicate the 3.0 km/s and 3.3 km/s move-out, respectively. Only the station pairs with SNR higher than 20 at 18 sec period are plotted here.

Figure 5. The average SNR for Raleigh and Love wave. Only station pairs separated by a distance greater than three wavelengths contributed to the average.

Figure 6. Phase velocity dispersion curves between stations CVS (Carmenet Vineyards, Sonoma, California) and VES (Vestal, Porterville, California), with various different values of the phase ambiguity factor N in equation (3). The inter-station distance is 409 km. The green dashed lines show the result with the value of N off by ±1. The solid red line shows the dispersion measurement obtained by FTAN and the black solid line is the reference dispersion curve.

Figure 7. (a) A diagram defining the inter-station distances d1, d2, and d3 used in the three-station analysis of the phase velocity measurements. (b) The relationship observed between Δd and Δt, where the red dots mark individual observations from station-triples. (c) The relationship between Δd and $\Delta t'$. (d) Same as (c), but λ=-π/4 is used.

Figure 8. (a) & (b) The histograms of Δt with λ=0 for Rayleigh and Love waves. The best fit Gaussian curves are also shown. (c) & (d) Same as (a) & (b), but λ=-π/4 is used for comparison.

Figure 9. (a) Location of stations O01C, R04C, ORV, and TIN. (b) The 5–40 sec band-pass filtered symmetric cross-correlations of the vertical–vertical component (Z-Z) and the transverse–transverse component (T-T). (c) The measured Rayleigh and Love wave dispersion curves based on the symmetric cross-correlations shown in (b). The reference dispersion curves for both Rayleigh and Love wave are shown as black solid and dashed lines respectively.

Figure 10. The number of phase velocity measurements satisfying the far-field approximation and the high SNR criterion are presented as a function of period. The results from the radial-radial (R-R), vertical-vertical (Z-Z), and transverse-transverse (T-T) cross-correlations are compared.

Figure 11. (a) & (c) The path coverage by the 12 sec Rayleigh and Love wave phase velocity data sets, respectively. (b) & (d) The 12 sec resolution maps for Rayleigh and Love waves, respectively, where resolution is defined as twice the standard deviation of a 2-D Gaussian function fit to the resolution matrix at each point. The 100 km resolution contour is shown with a thick black line.

Figure 12. The estimated Rayleigh wave phase velocity maps at periods of 8 sec, 12 sec, 16 sec, and 20 sec. The 100 km resolution contour is shown for reference.

Figure 13. The estimated Love wave phase velocity maps at periods of 8 sec, 12 sec, 16 sec, and 20 sec. The 100 km resolution contour is shown for reference.

Figure 14. Travel time misfit histograms for the tomography maps shown in Figures 12 and 13. The standard deviation (STDV) of misfit is also presented.

Figure 15. Vertical phase velocity sensitivity kernels of Rayleigh and Love waves at periods of 8, 12, 16, and 20 sec, calculated with the 1D PREM model in which the ocean is replaced by a sedimentary layer.

Figure 16. An example of iso-phase hyperbolas each separated from its nearest neighbor by $\pm\pi$. A phase velocity of 3 km/s for 50 sec period is used to construct the hyperbolas. The same setup parameters were used for the synthetic experiments. The gray area defines the region over which sources were randomly distributed for the synthetic experiment referred to as Case 3.

Figure 17. (a) The synthetic cross-correlations for Cases 1, 2 and 3. (b) The phase velocity dispersion curves result from the estimated Green's functions derived from the synthetic cross-correlations in (a). Two initial phase values, 0 and $\pi/4$, are used to obtain the phase velocity

dispersion curve for Case 2. In general, the correct phase velocity, 3 km/s, is returned when the correct initial phase is applied. (c) The measured group velocity dispersion curves for Cases 1, 2, and 3.

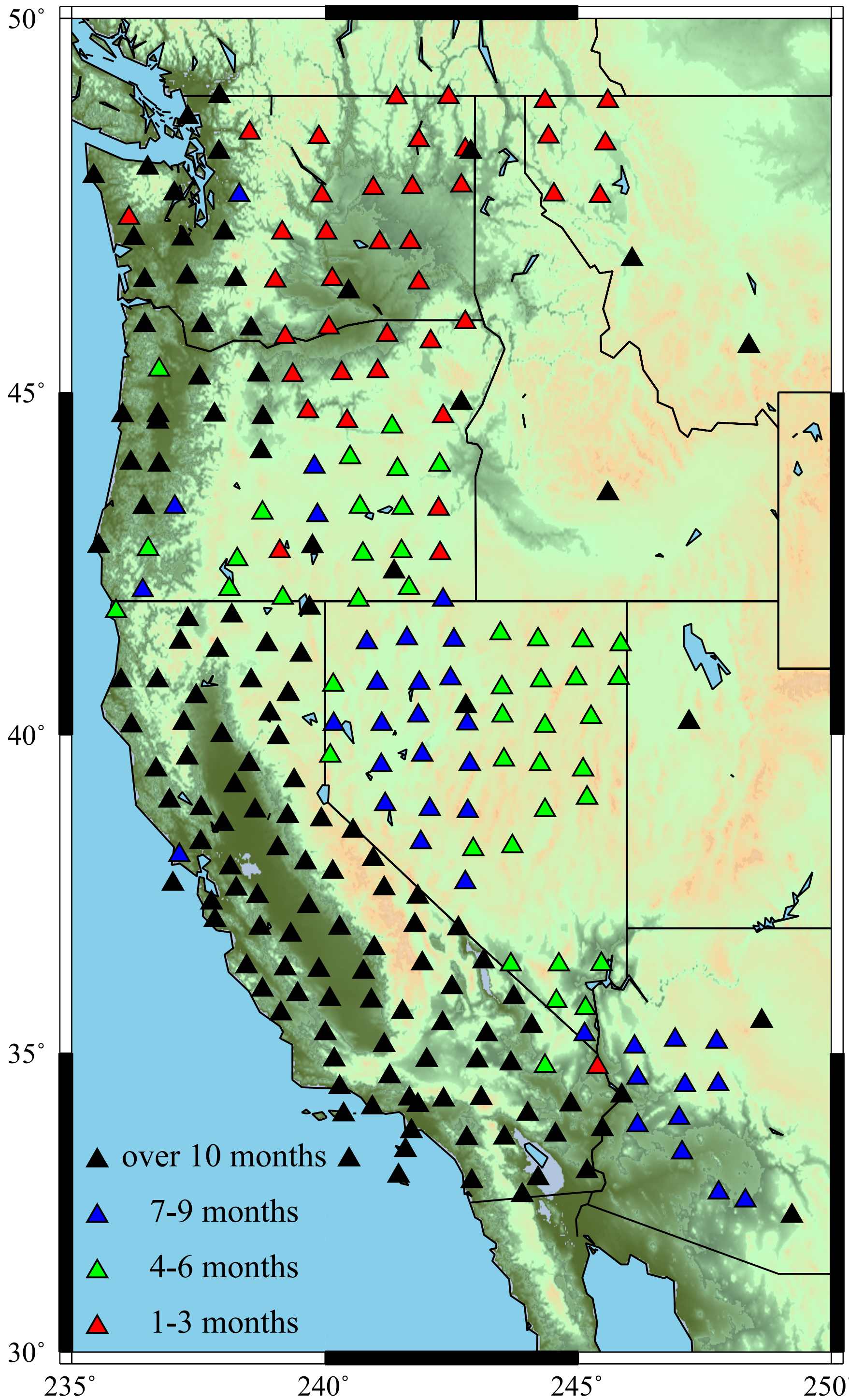
50°
45°
40°
35°
30°
235°
240°
245°
250°
over 10 months
7-9 months
4-6 months
1-3 months

Figure 1.

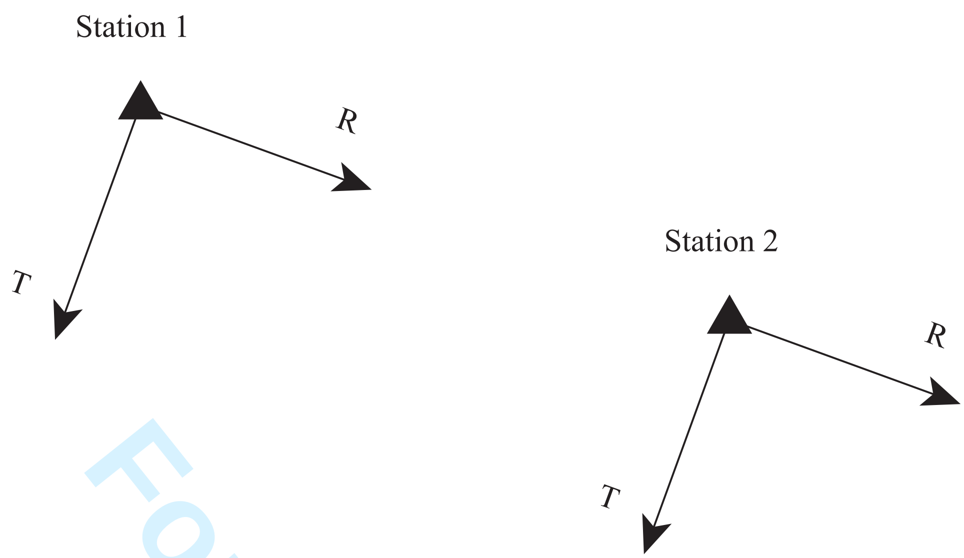

Figure 2.

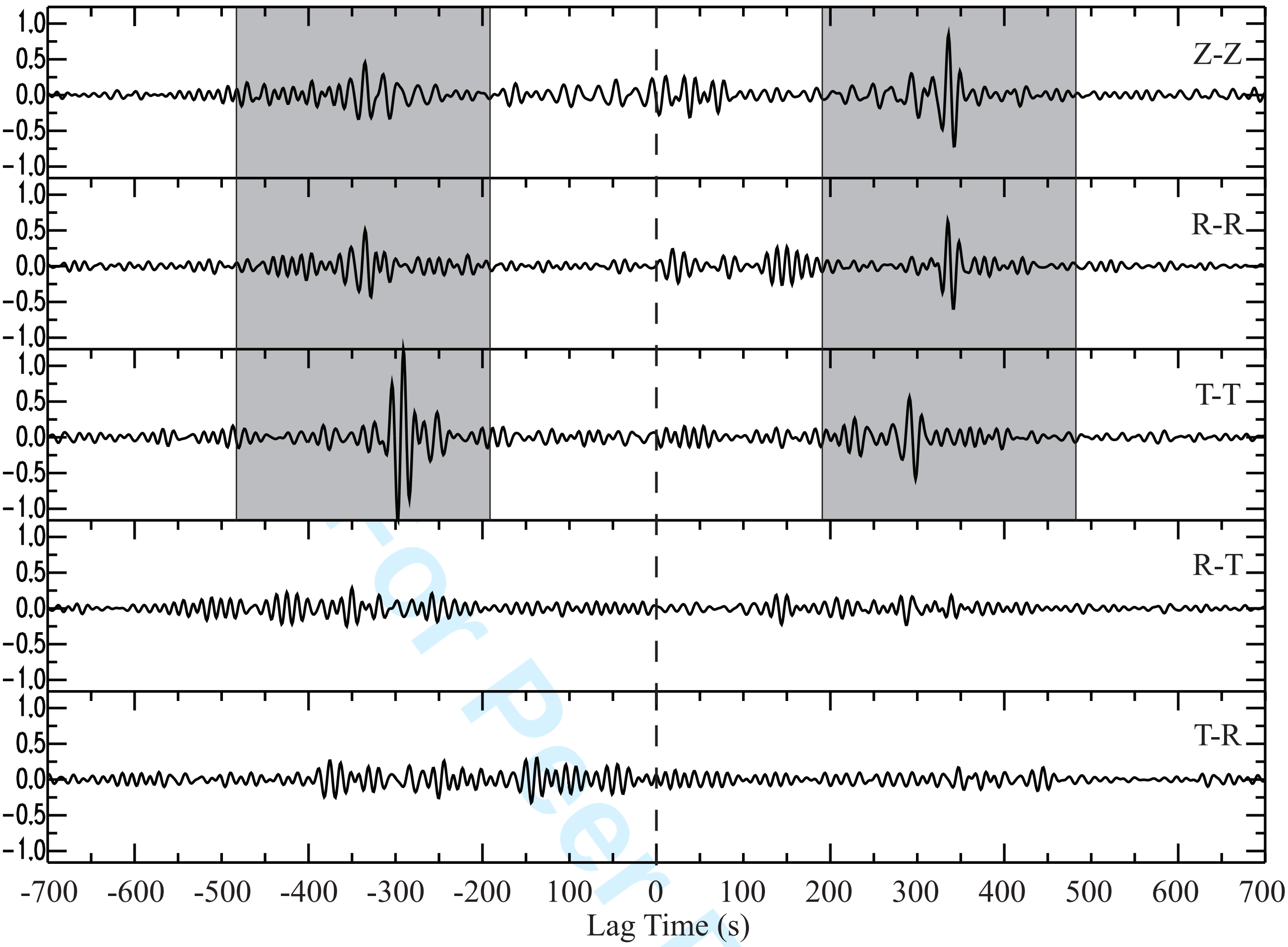
Z-Z
R-R
T-T
R-T
T-R
1.0
0.5
0.0
-0.5
-1.0
-700 -600 -500 -400 -300 -200 100 0 100 200 300 400 500 600 700
Lag Time (s)

Figure 3

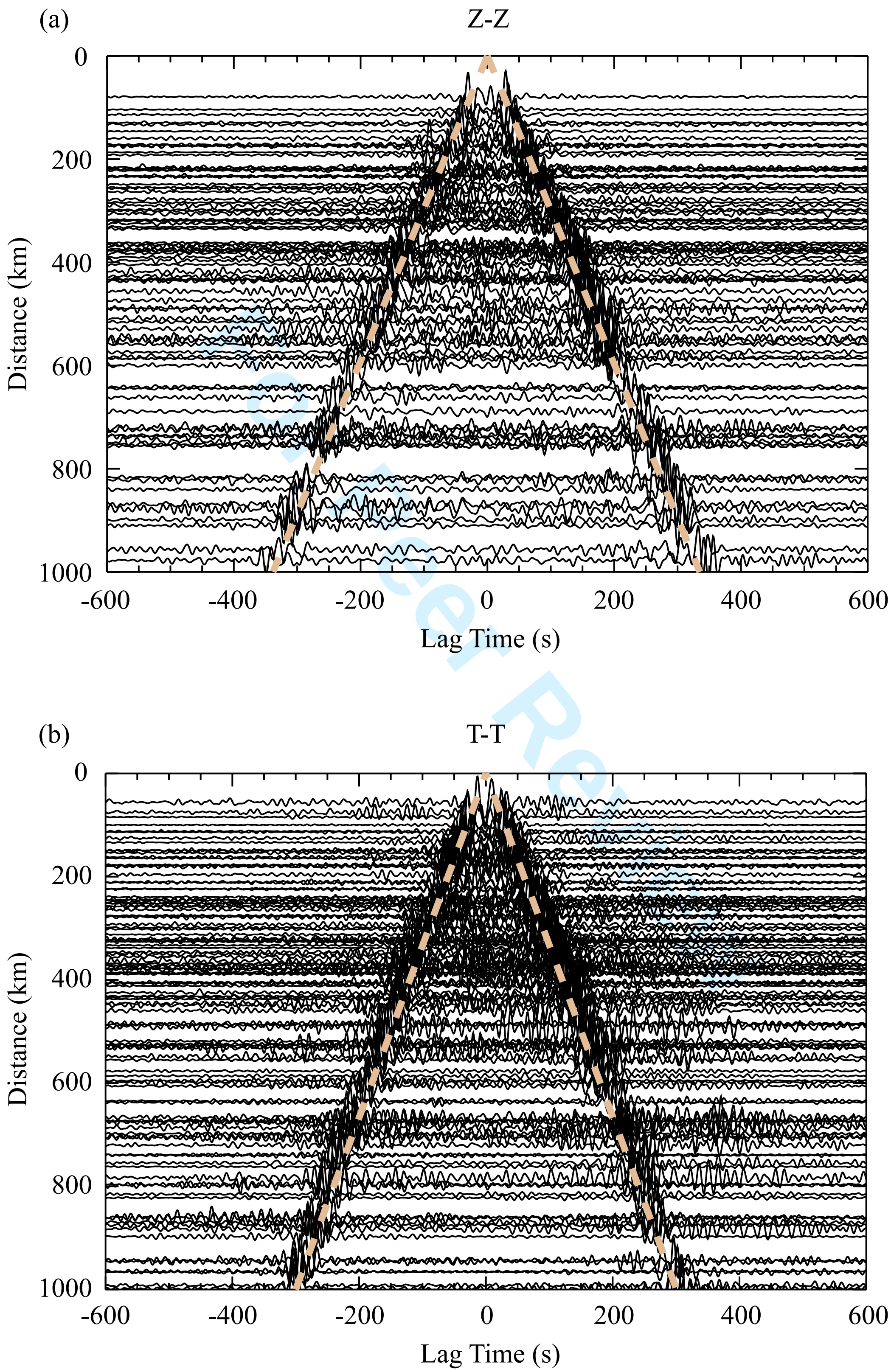
(a)
Z-Z
Distance (km)
0
200
400
600
800
1000
-600
-400
-200
0
200
400
600
Lag Time (s)
(b)
T-T
Distance (km)
0
200
400
600
800
1000
-600
-400
-200
0
200
400
600
Lag Time (s)

Figure 4.

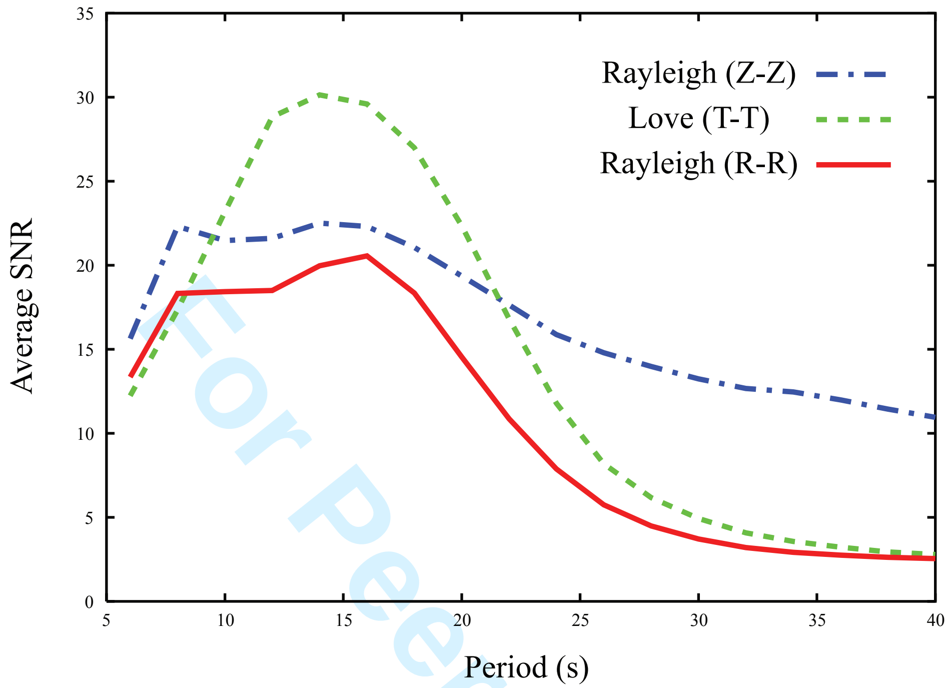
Rayleigh (Z-Z)
Love (T-T)
Rayleigh (R-R)
Average SNR
Period (s)
0
5
10
15
20
25
30
35
5
10
15
20
25
30
35
40

Figure 5

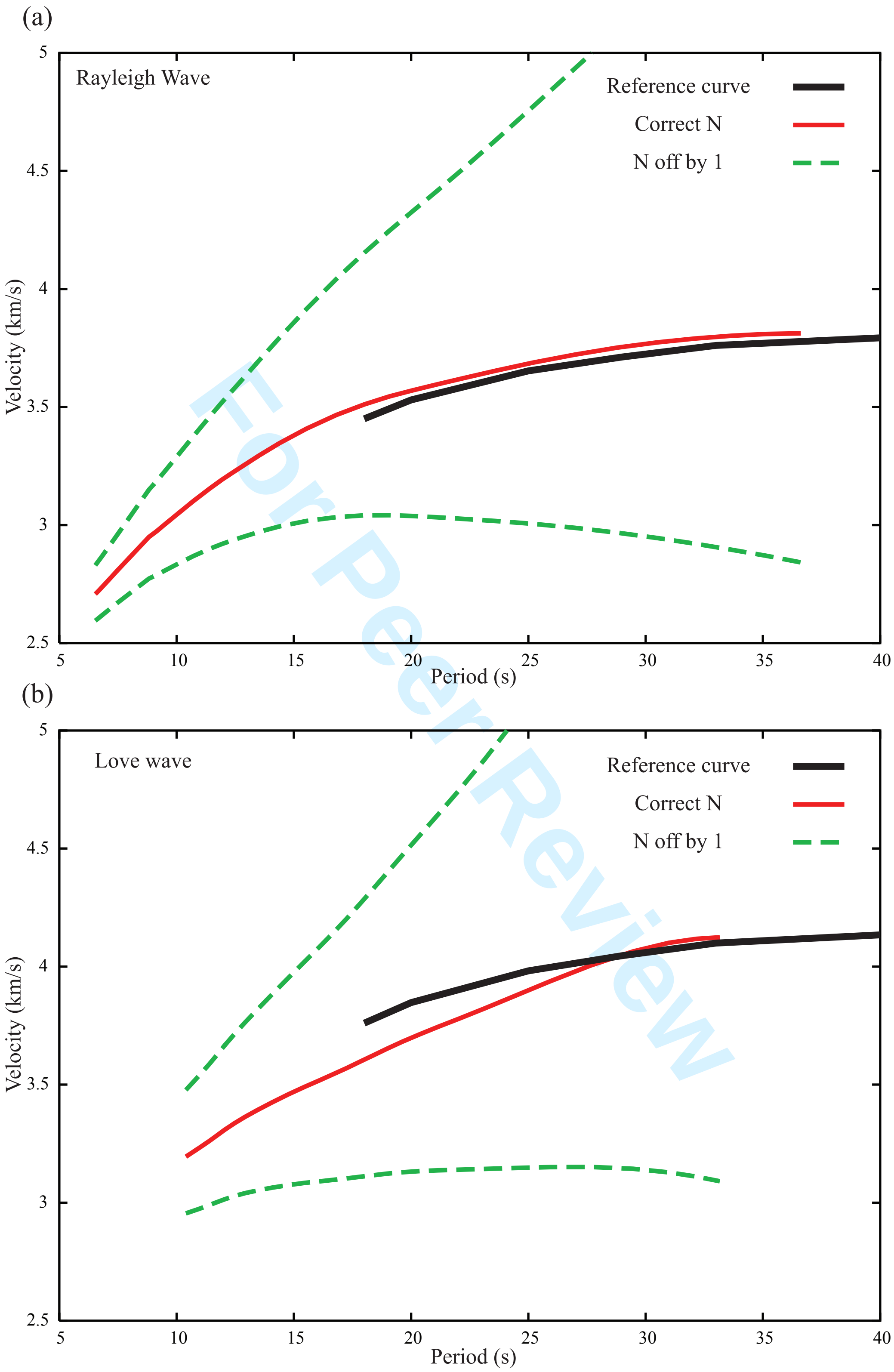
(a)
Rayleigh Wave
Reference curve
Correct N
N off by 1
Velocity (km/s)
Period (s)
5
4.5
4
3.5
3
2.5
5
10
15
20
25
30
35
40
(b)
Love wave
Reference curve
Correct N
N off by 1
Velocity (km/s)
Period (s)

Figure 6.

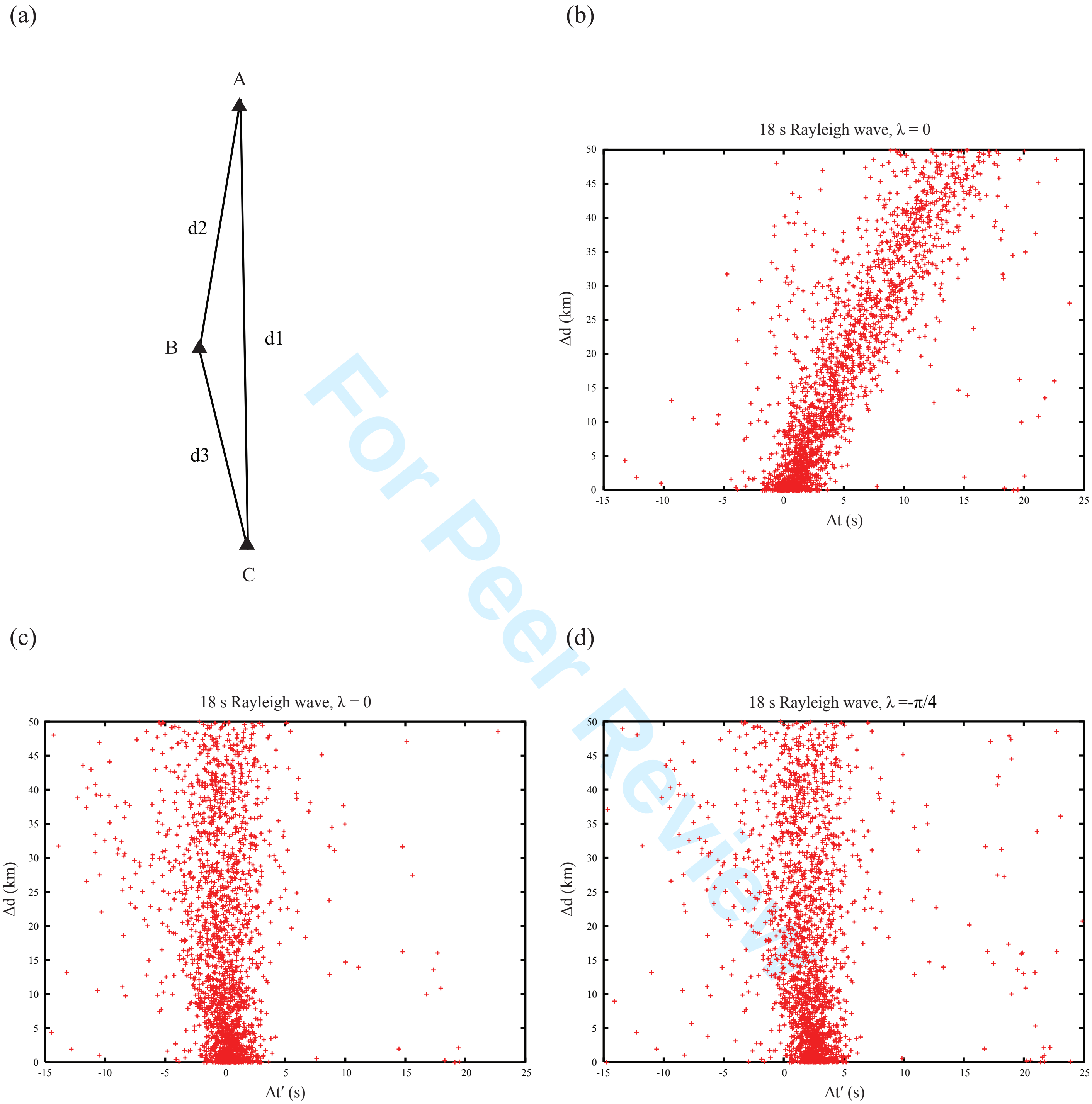
(a)
A
B
C
d1
d2
d3
(b)
18 s Rayleigh wave, λ = 0
Δd (km)
Δt (s)
(c)
18 s Rayleigh wave, λ = 0
Δd (km)
Δt′ (s)
(d)
18 s Rayleigh wave, λ =-π/4
Δd (km)
Δt′ (s)

Figure 7

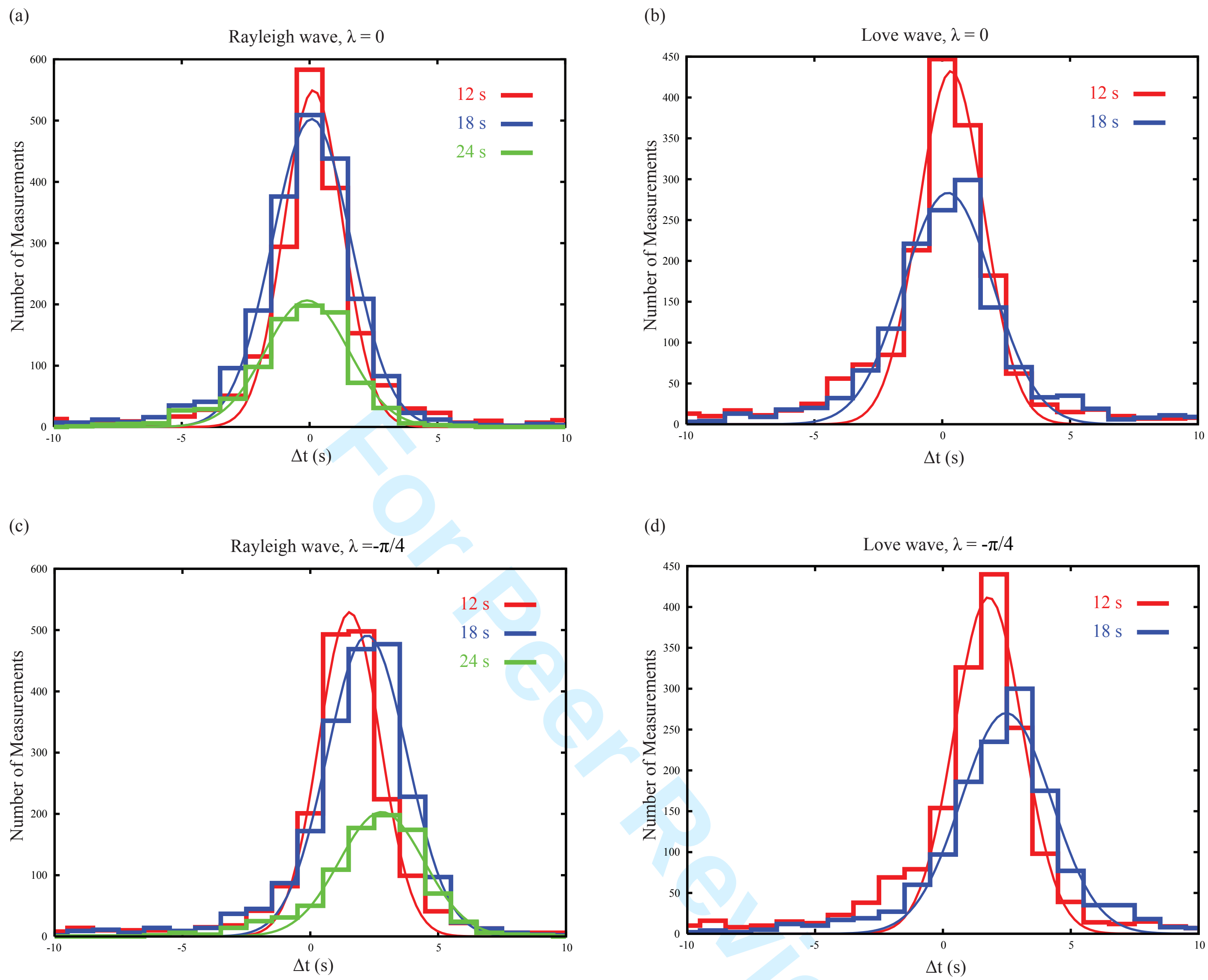
(a)
Rayleigh wave, λ = 0
Number of Measurements
Δt (s)
12 s
18 s
24 s
(b)
Love wave, λ = 0
Number of Measurements
Δt (s)
12 s
18 s
(c)
Rayleigh wave, λ =-π/4
Number of Measurements
Δt (s)
12 s
18 s
24 s
(d)
Love wave, λ = -π/4
Number of Measurements
Δt (s)
12 s
18 s

Figure 8.

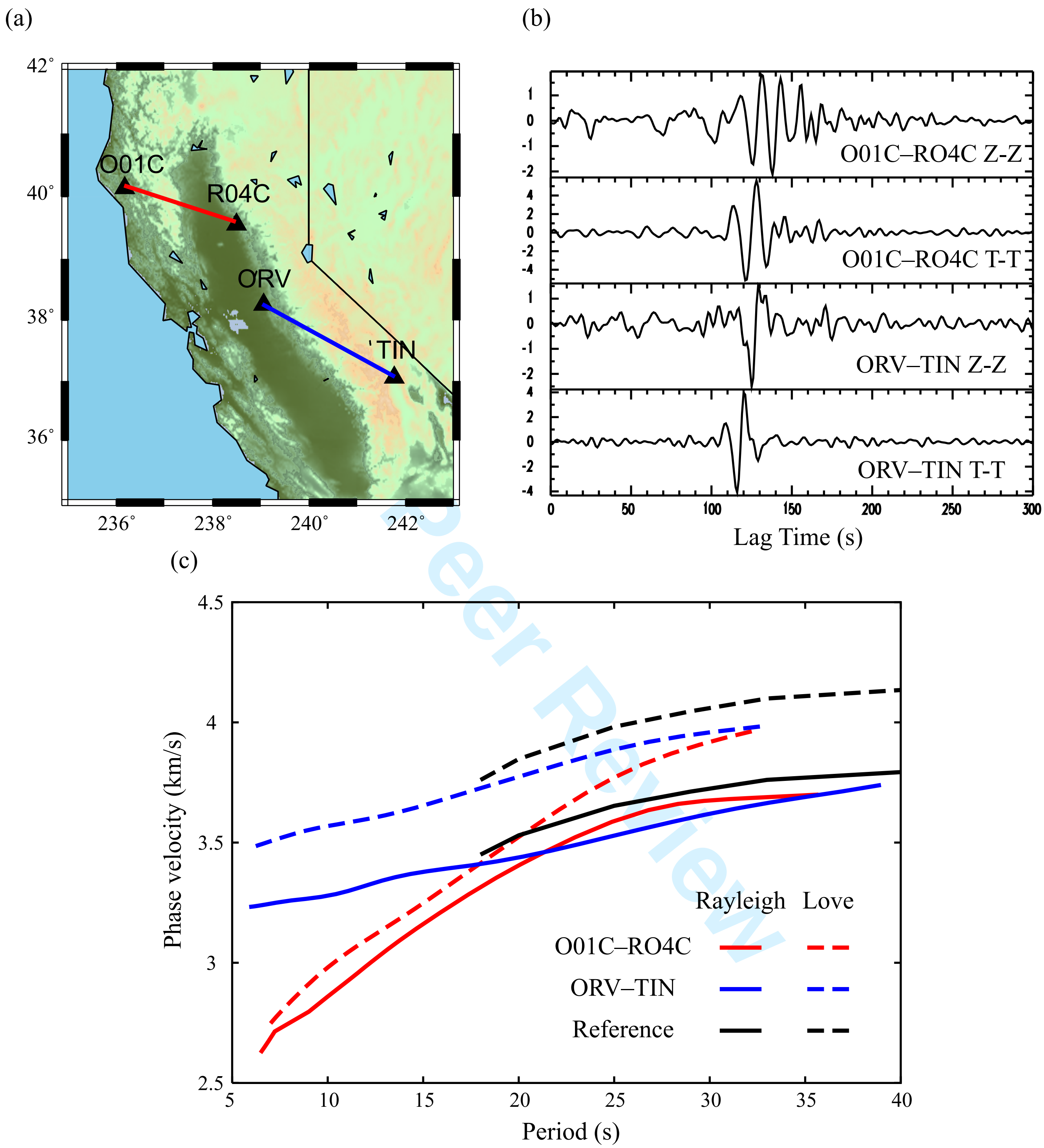
(a)
42˚
40˚
38˚
36˚
236˚
238˚
240˚
242˚
O01C
R04C
ORV
TIN
(b)
O01C–RO4C Z-Z
O01C–RO4C T-T
ORV–TIN Z-Z
ORV–TIN T-T
0
50
100
150
200
250
300
Lag Time (s)
(c)
Phase velocity (km/s)
4.5
4
3.5
3
2.5
5
10
15
20
25
30
35
40
Period (s)
Rayleigh
Love
O01C–RO4C
ORV–TIN
Reference

Figure 9.

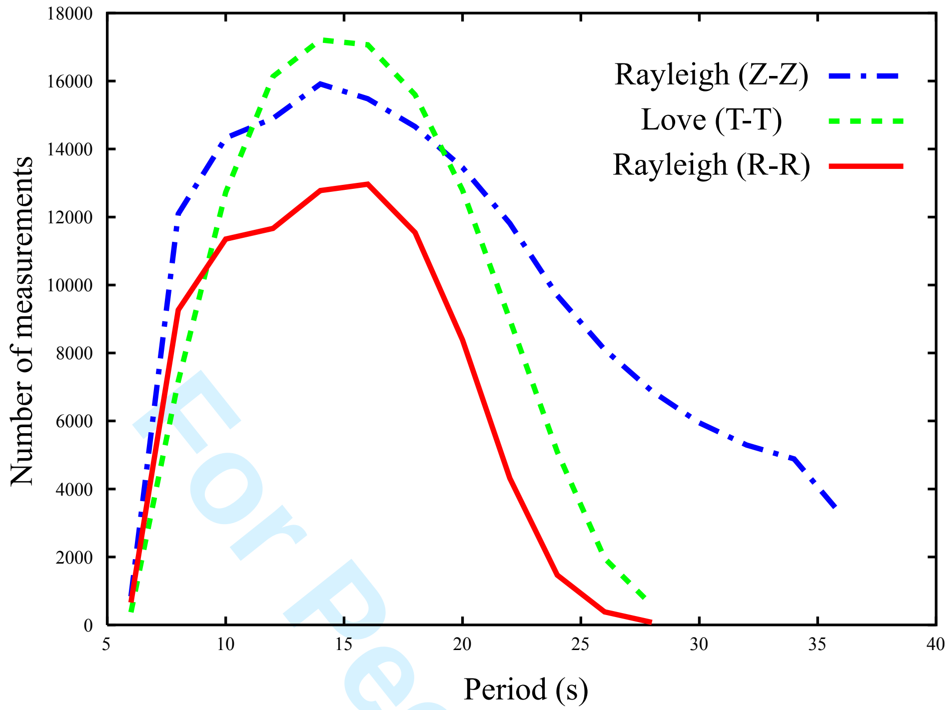

Number of measurements
Period (s)
Rayleigh (Z-Z)
Love (T-T)
Rayleigh (R-R)
0
2000
4000
6000
8000
10000
12000
14000
16000
18000
5
10
15
20
25
30
35
40

Figure 10.

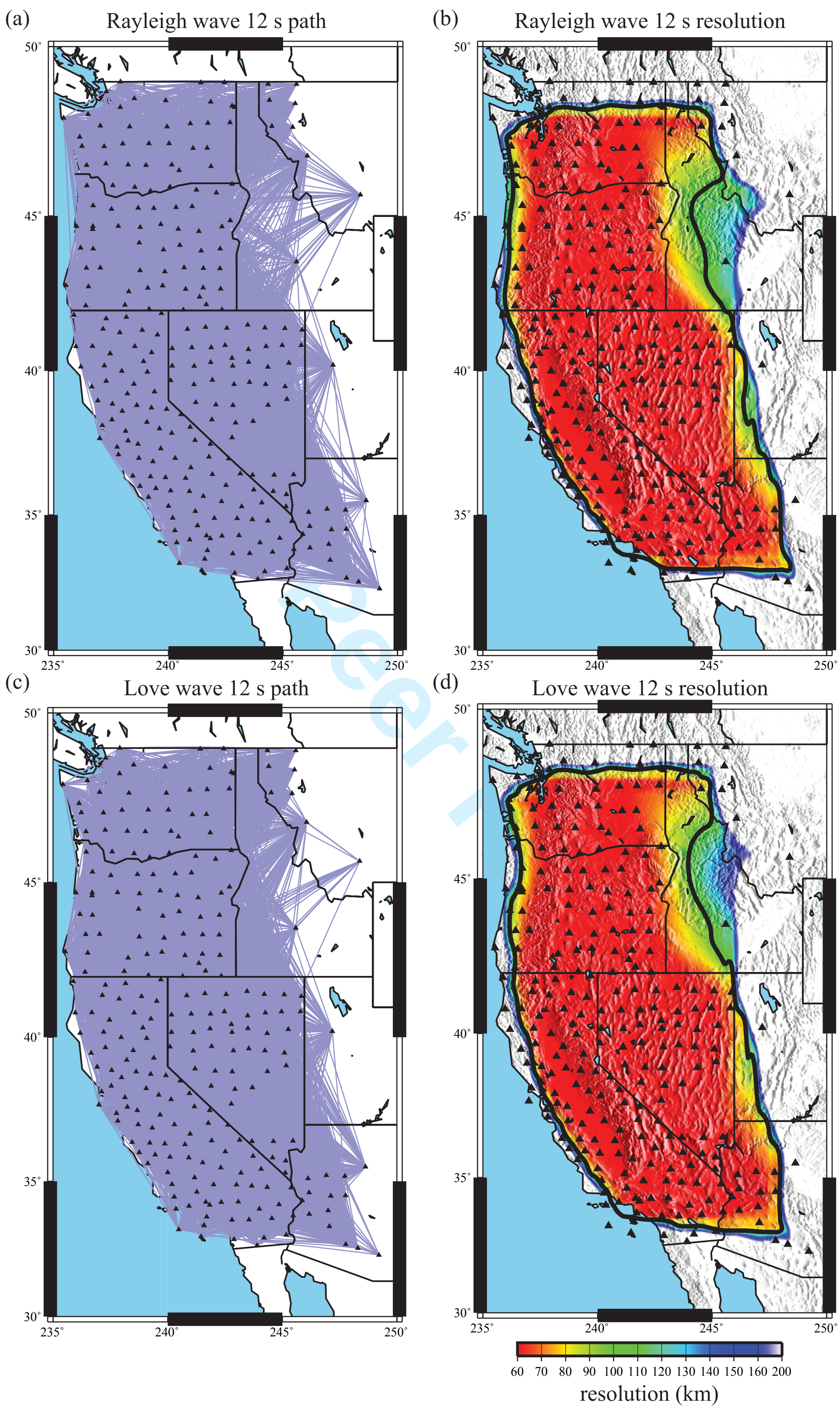
(a)
Rayleigh wave 12 s path
(b)
Rayleigh wave 12 s resolution
(c)
Love wave 12 s path
(d)
Love wave 12 s resolution
50°
45°
40°
35°
30°
235°
240°
245°
250°
60 70 80 90 100 110 120 130 140 150 160 200
resolution (km)

Figure 11.

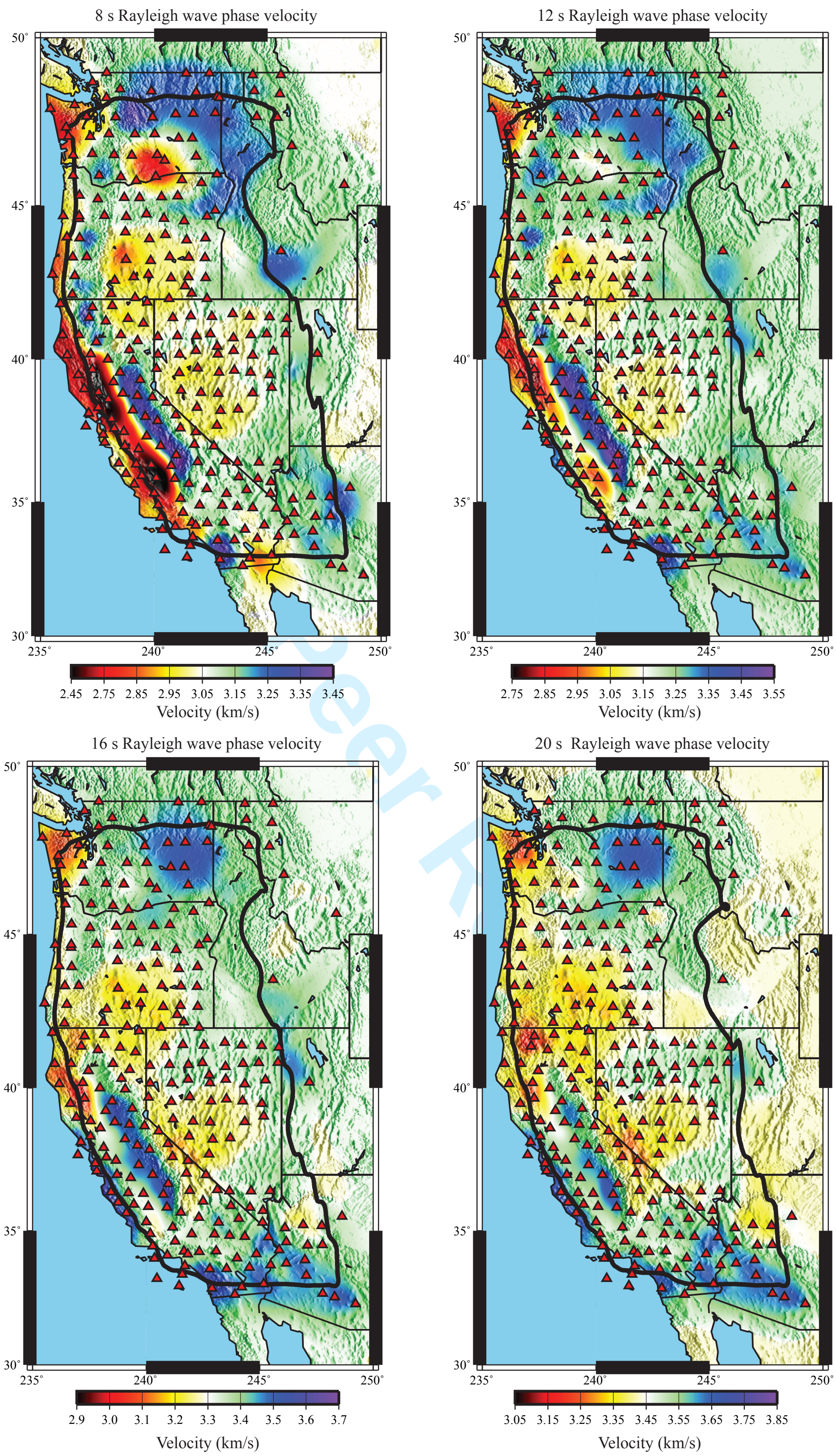
8 s Rayleigh wave phase velocity
12 s Rayleigh wave phase velocity
16 s Rayleigh wave phase velocity
20 s Rayleigh wave phase velocity
50° 45° 40° 35° 30°
235° 240° 245° 250°
2.45 2.75 2.85 2.95 3.05 3.15 3.25 3.35 3.45
2.75 2.85 2.95 3.05 3.15 3.25 3.35 3.45 3.55
2.9 3.0 3.1 3.2 3.3 3.4 3.5 3.6 3.7
3.05 3.15 3.25 3.35 3.45 3.55 3.65 3.75 3.85
Velocity (km/s)

Figure 12

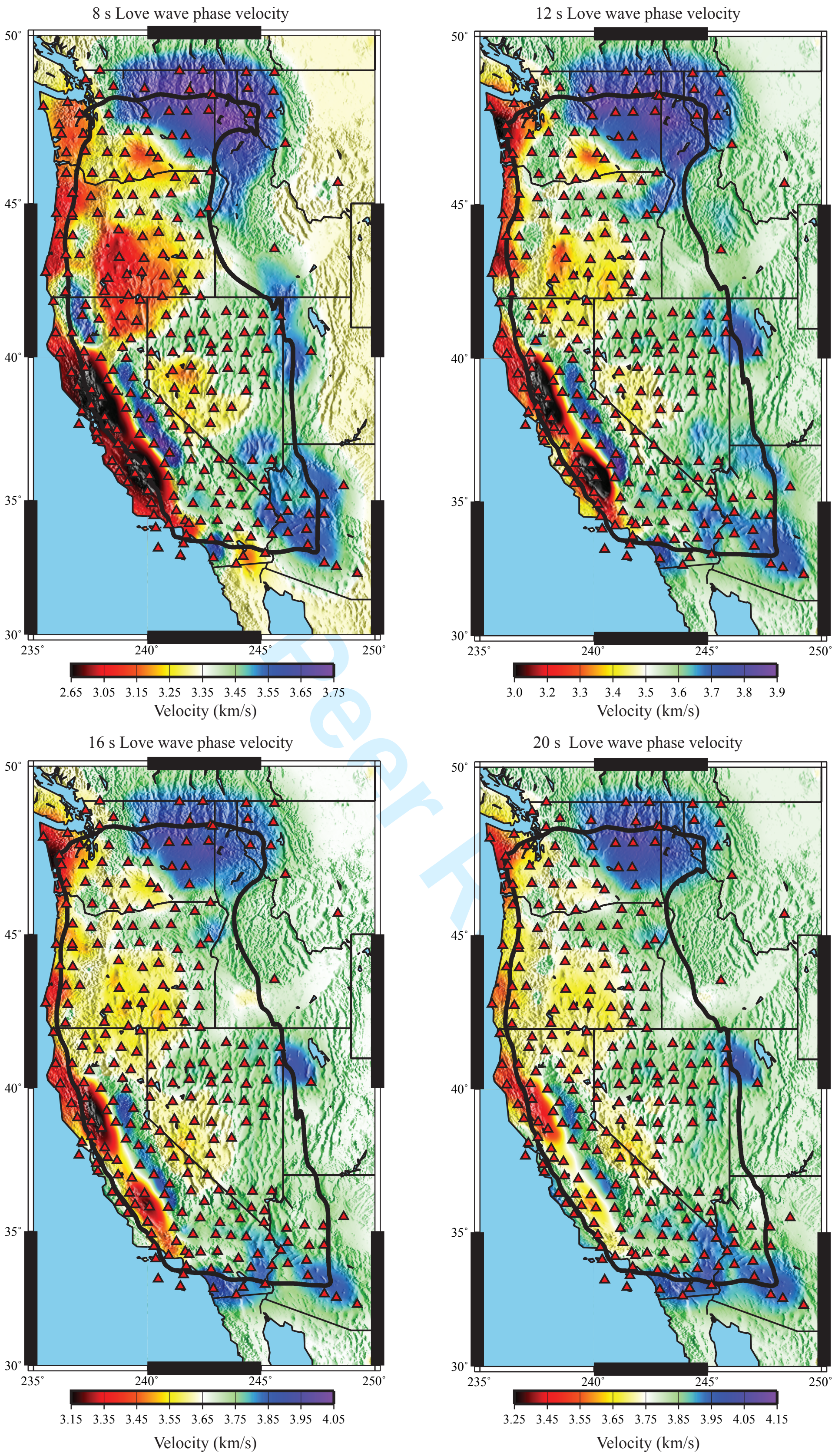
8 s Love wave phase velocity
50° 45° 40° 35° 30°
235° 240° 245° 250°
2.65 3.05 3.15 3.25 3.35 3.45 3.55 3.65 3.75
Velocity (km/s)
12 s Love wave phase velocity
50° 45° 40° 35° 30°
235° 240° 245° 250°
3.0 3.2 3.3 3.4 3.5 3.6 3.7 3.8 3.9
Velocity (km/s)
16 s Love wave phase velocity
50° 45° 40° 35° 30°
235° 240° 245° 250°
3.15 3.35 3.45 3.55 3.65 3.75 3.85 3.95 4.05
Velocity (km/s)
20 s Love wave phase velocity
50° 45° 40° 35° 30°
235° 240° 245° 250°
3.25 3.45 3.55 3.65 3.75 3.85 3.95 4.05 4.15
Velocity (km/s)

Figure 13

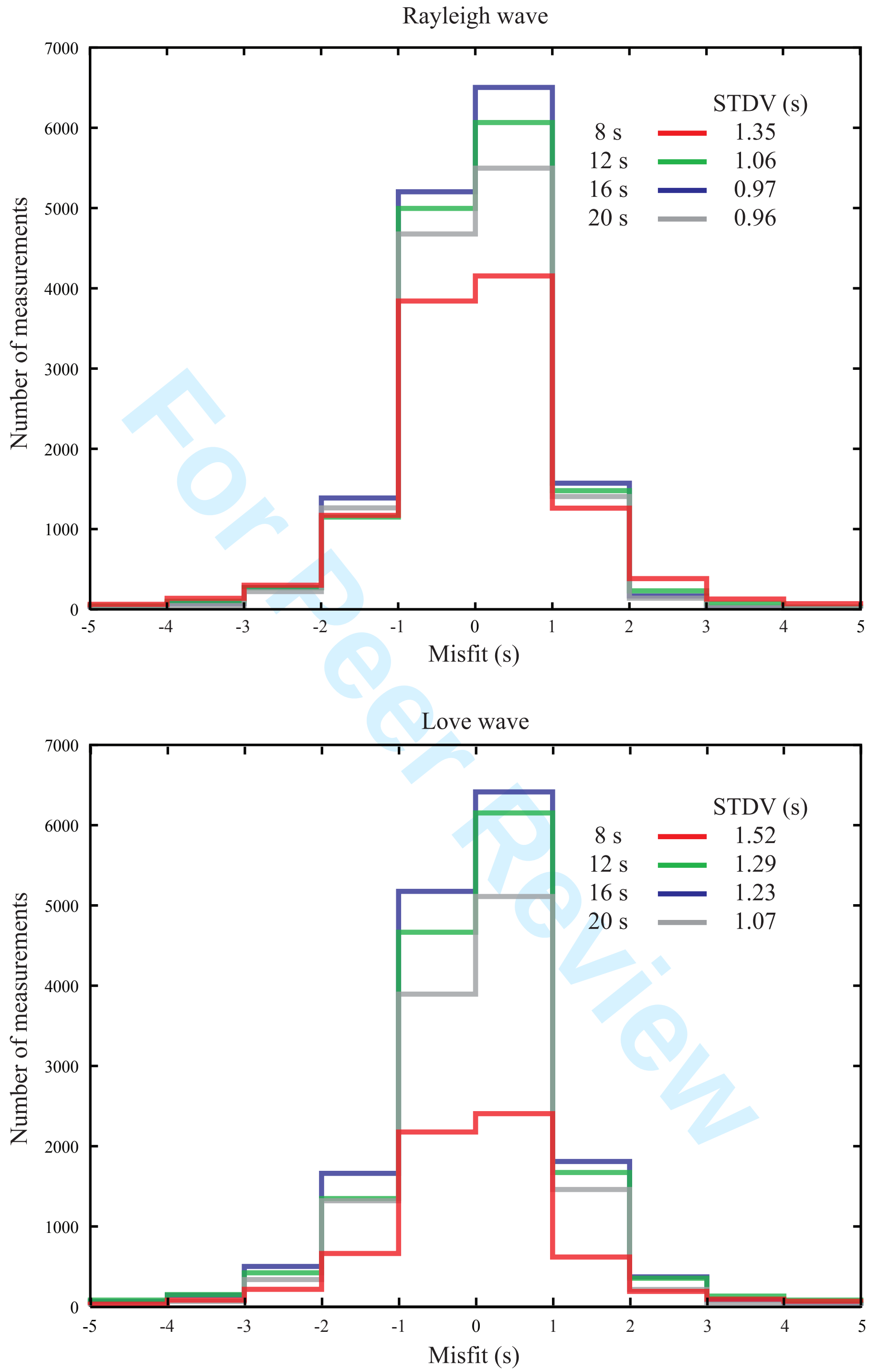
Rayleigh wave
Number of measurements
Misfit (s)
STDV (s)
8 s 1.35
12 s 1.06
16 s 0.97
20 s 0.96
Love wave
Number of measurements
Misfit (s)
STDV (s)
8 s 1.52
12 s 1.29
16 s 1.23
20 s 1.07

Figure 14

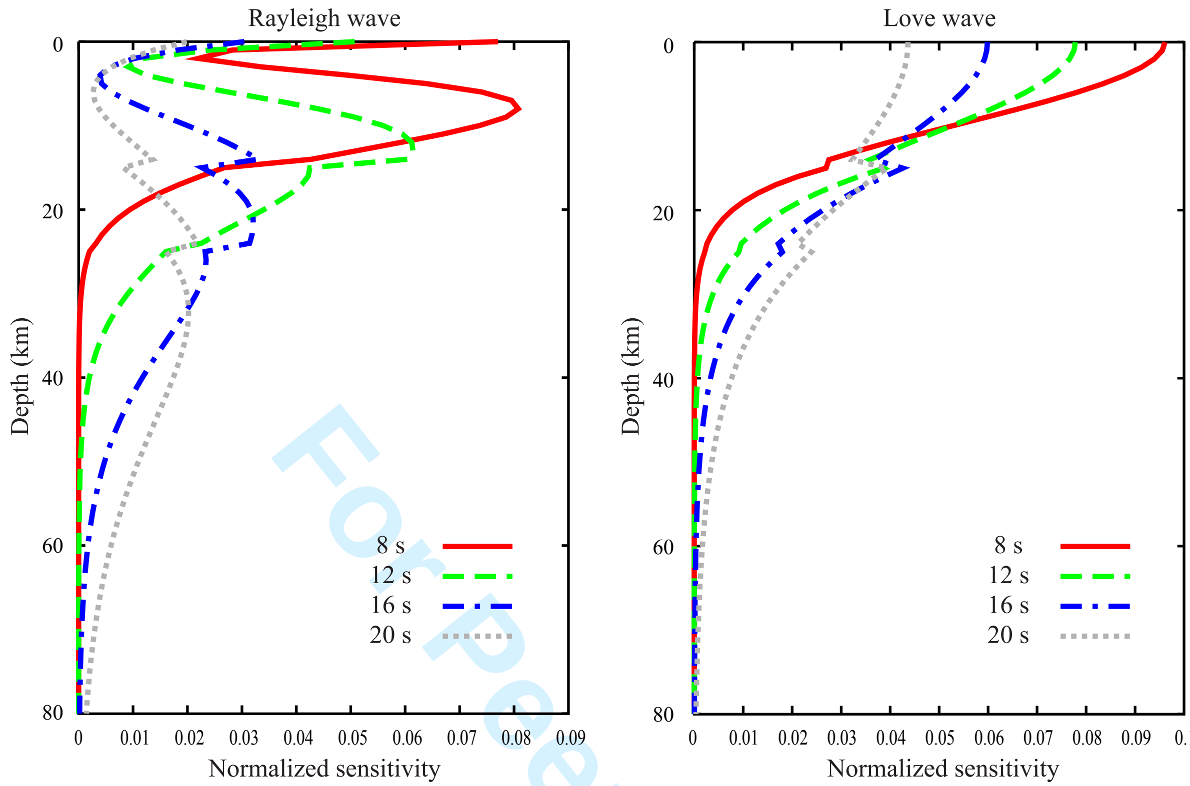
Rayleigh wave
Love wave
Depth (km)
Normalized sensitivity
0
20
40
60
80
0
0.01
0.02
0.03
0.04
0.05
0.06
0.07
0.08
0.09
0.1
8 s
12 s
16 s
20 s

Figure 15

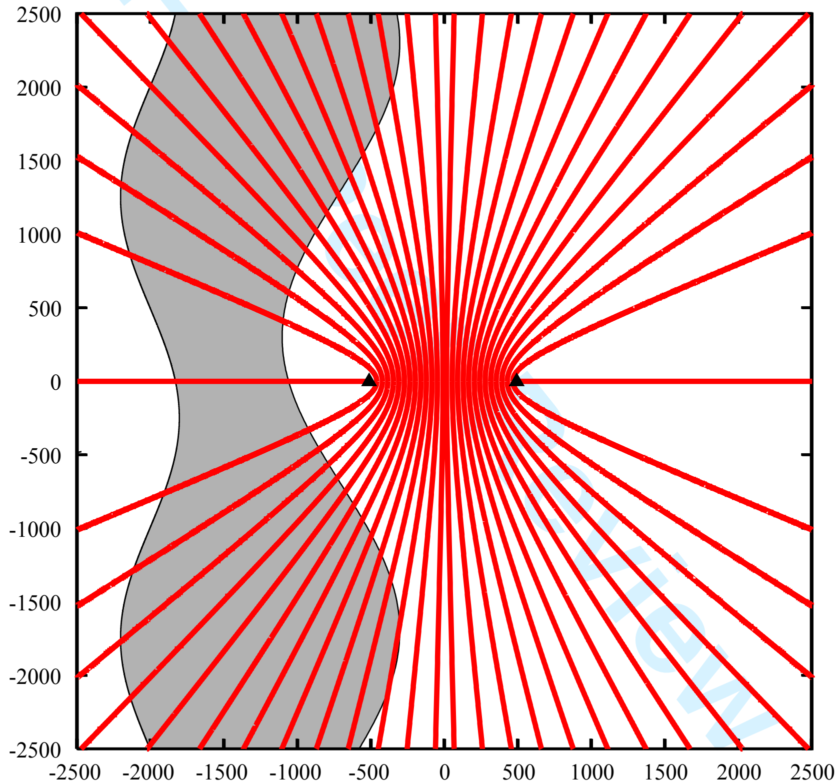
2500
2000
1500
1000
500
0
-500
-1000
-1500
-2000
-2500
-2500
-2000
-1500
-1000
-500
0
500
1000
1500
2000
2500

Figure 16.

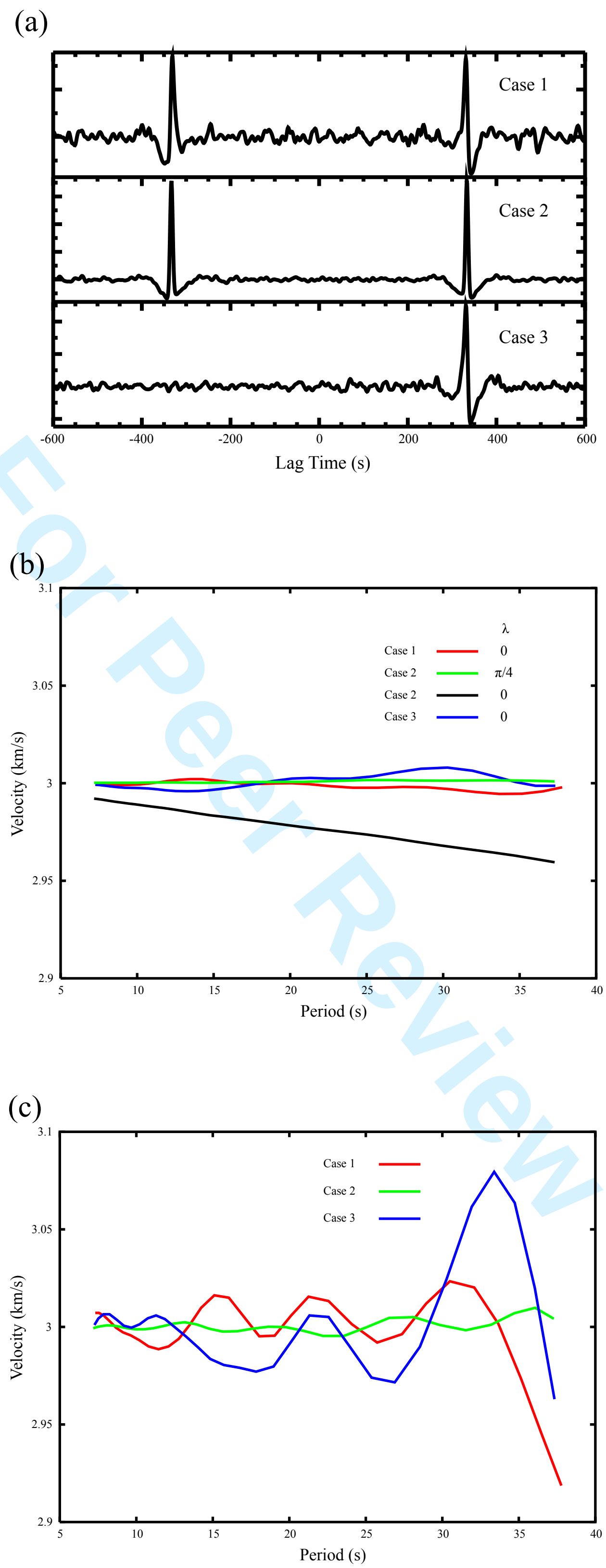
(a)
Case 1
Case 2
Case 3
-600
-400
-200
0
200
400
600
Lag Time (s)
(b)
λ
Case 1 0
Case 2 π/4
Case 2 0
Case 3 0
Velocity (km/s)
3.1
3.05
3
2.95
2.9
5
10
15
20
25
30
35
40
Period (s)
(c)
Case 1
Case 2
Case 3
Velocity (km/s)
Period (s)

Figure 17.

Table 1.

	Rayleigh Wave						Love Wave			
	λ=0			λ=-π/4			λ=0		λ=-π/4	
	12 s	18 s	24 s	12 s	18 s	24 s	12 s	18 s	12 s	18 s
Δt_{mean} (s)	0.151	0.084	-0.097	1.541	2.226	2.793	0.349	0.224	1.785	2.477
σ (s)	1.148	1.536	1.623	1.199	1.561	1.654	1.277	1.753	1.337	1.765